Bull Volcanol (2003) 65:144–164
DOI 10.1007/s00445-002-0250-1

RESEARCH ARTICLE

Armin Freundt

Entrance of hot pyroclastic flows into the sea: experimental observations

Received: 14 February 2001 / Accepted: 24 September 2002 / Published online: 26 November 2002

Abstract The entrance of hot pyroclastic flows into water has been observed in a series of experiments in which shooting granular flows of hot ignimbrite ash (≤403 °C), of bulk density near that of water, run down a smooth chute and enter a water-filled tank at an angle of 26°. Flows of relatively cool ash (<150 °C) impulsively displace some volume of near-shore water upon impact, generating a water wave that rapidly travels away from shore. The granular flow material then separates into two portions. (1) A fine-ash surge cloud is formed where the granular flow hits water and rapidly travels down-tank over the water. (2) The main portion of material penetrates the surface and mixes with the water, creating a turbulent mixing zone resembling a hydraulic jump, which advances downstream as long as the pyroclastic flow is maintained. Most pumice floats to the surface, lithics and coarse ash fall out onto the floor, but ash that remains in suspension forms a turbidity current that travels down the floor of the tank. With increasing ash temperature, an increasing fraction of incoming material is initially transported along the water surface; almost all material takes this path at temperatures >250 °C. Mixing across the water surface over some distance from shore generates steam explosions forming fountains of wet and dry ash and convectively rising fine-ash plumes. Steam explosions increase in strength and lateral extent towards higher ash temperatures and mass fluxes. The explosions generate water waves that remain driven by massive fountain fallout across some distance from shore. The ash fountains feed pyroclastic surges, which advance down tank over water at high speeds. Underwater plumes of sediment falling from the ash fountains and surges drop coarse load onto the floor whereas the finer load forms a turbidity current. High temperature and poor size sorting of pyroclastic flows are key parameters that determine the processes of interaction with water and the associated hazards. Poor sorting allows for the formation of ash-cloud surges moving over water, even from cool flows. High temperatures cause littoral explosions and facilitate extensive mass transport over water. All flows generate tsunami waves by different mechanisms.

Electronic supplementary material (two movies) is available if you access this article at http://dx.doi.org/10.1007/s00445-002-0250-1. On that page (frame on the left side), a link takes you directly to the supplementary material.

Keywords Ash-cloud surge · Hot ash–water mixing · Littoral explosion · Pyroclastic flow · Tsunami · Turbidity current

Editorial responsibility: T.H. Druitt

Electronic supplementary material (two movies) is available if you access this article at http://dx.doi.org/10.1007/s00445-002-0250-1. On that page (frame on the left side), a link takes you directly to the supplementary material.

A. Freundt (✉)
GEOMAR Research Center for Marine Geosciences,
Wischhofstr. 1–3, 24148 Kiel, Germany
e-mail: afreundt@geomar.de
Tel.: +49-431-6002131
Fax: +49-431-6002924

Introduction

Many explosive volcanoes that produce pyroclastic flows are situated near the sea (or lakes or rivers), especially those in subduction-zone and ocean-island settings. Pyroclastic flows generated at near-shore volcanoes can enter the sea and produce widespread submarine volcaniclastic deposits. Geologic evidence, reviewed by Cas and Wright (1991), suggests a variety of ways in which pyroclastic flows interact with the sea (Fig. 1):

- Diving of dense flows into water and transformation into water-supported debris flows and turbidity currents is supported by most geologic evidence (Cas and Wright 1991; Carey 2000). The volcaniclastic apron around Gran Canaria, for example, is largely composed of volcaniclastic turbidite beds extending up to 750 km from coast, which can be correlated with

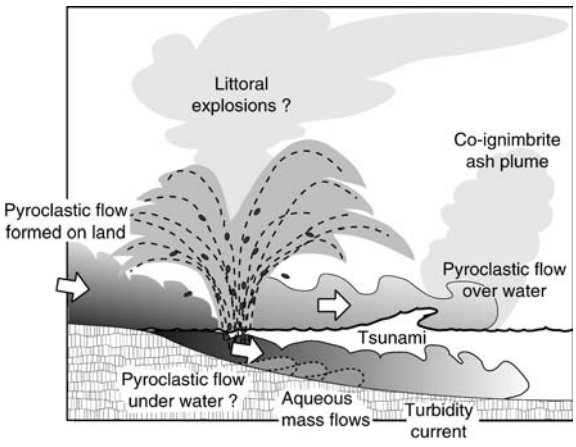

Fig. 1 Schematic illustration of interaction scenarios where pyroclastic flows generated on land enter the sea. The near-shore area of interaction is the focus of this study. *?* Processes for which geologic evidence is uncertain

ignimbrites on land (Freundt and Schmincke 1998; Schmincke and Sumita 1998).

- Slowing and welding pyroclastic flows push the water back from the shoreline, accompanied by minor disintegration at the front and at the contact to wet sediment, and probably occurred during near-shore emplacement of ancient welded ignimbrites intercalated with marine sediments (e.g., Reedman et al. 1987; Fritz and Stillman 1996).
- Flow of low-density pyroclastic currents over water; the Koya flow in Japan, for example, had to cross 30 km over the deep waters of the Japanese sea to be emplaced on Kyushu and neighboring islands and lost much of its denser load during this passage (Ui et al. 1983).
- Explosive disintegration near shore; Walker (1979) interpreted widespread fallout tephra at the north coast of New Zealand to have resulted from littoral explosions where a major pyroclastic flow entered the sea, but re-investigation showed that this tephra was produced by an independent eruption (C.J.N. Wilson personal communication). Whitham (1989) implied intense fragmentation of pyroclasts upon entry into the sea from higher crystal/lithic ratios in submarine versus on-land pyroclastic flow deposits, but evidence for coastal explosions is not commonly reported.

Direct geologic evidence of pyroclastic flow – water interaction is rarely preserved due to highly erosive wave action in the near-shore environment. The entrance of pyroclastic flows into the sea has been witnessed, for example, by the Romans during the 79 A.D. eruption of Vesuvius (Sigurdsson et al. 1982) and, more recently, during the 1996–1999 eruptions of Soufriere Hills volcano on Montserrat (Cole et al. 1998). Probably the best-documented example of pyroclastic flows interacting with the sea is the 1883 Krakatau eruption, which is fairly well constrained by eye-witness accounts and geologic studies (Mandeville et al. 1994, 1996; Carey et al. 1996, 2000). During a period of 2 days, a series of pyroclastic flows entered the sea and deposited hot (475–500 °C), massive tuff on the seafloor around the island in water depths of about 20–60 m and to more than 15 km from the source caldera. Dilute pyroclastic density currents traveled over the sea, left massive through stratified deposits on overrun islands, and caused burn fatalities on the southern Sumatra coast 40 km from vent before they became sufficiently dilute to rise as wet ash plumes producing mud rain. Which of the many coupled air–sea waves and tsunamis, which killed 35,000 people along the Sunda Strait coast, were generated by the entrance of pyroclastic flows into the sea, as opposed to generation by submarine explosion or partial collapse of the volcanic edifice, is still a subject of discussion (Francis 1985; Yokoyama 1987; Nomanbhjoy and Satake 1995; Carey et al. 2001).

Previous experimental studies on intrusive gravity currents using pure or particle-laden liquids have identified general fluid dynamic aspects of intrusion such as the degree of mixing with the ambient medium or the waveforms generated as a function of flow rate and density contrast (Rottman and Simpson 1989; Cas et al. 1998). Legros and Druitt (2000) quantified the shoreline displacement as water is pushed back by an intruding liquid flow. McLeod et al. (1999) used particle-laden liquid flows to study the mixing upon entry into water as a function of density contrast and sedimentation. Such studies provide important fluid-dynamical insights, but do not capture the effects of high temperatures and poor sorting of pyroclastic material and of three-phase (gas, liquid, solids) flow that are expected to be important in the case of natural pyroclastic flows entering the sea. This paper reports experiments in which hot grain flows of natural ignimbrite ash flow into a tank filled with water. Phenomena observed with poorly-sorted ash are described here; the effects of variable grain size distributions, the nature of resulting deposits, and insights into interaction processes gained from ongoing high-speed filming will be reported elsewhere.

Experimental setup and scaling

Setup

The basic setup was simple (Fig. 2): flows of hot ignimbrite ash ran down a chute into a water-filled tank that was 303 cm long, 48 cm high, and 36 cm wide; a second, inner line of heat-resistant panes left a usable width of 19.5 cm. Pre-dried and weighed ash was heated in a furnace and then transferred into a stainless-steel funnel, which was lifted atop the head of a steel chute (Fig. 2). Ash temperature in the funnel was monitored by a built-in thermocouple and, after cooling to the desired temperature, the hatch at funnel bottom was quickly opened and the ash flowed out onto the smooth stainless-steel chute with a rectangular cross section and inclined at

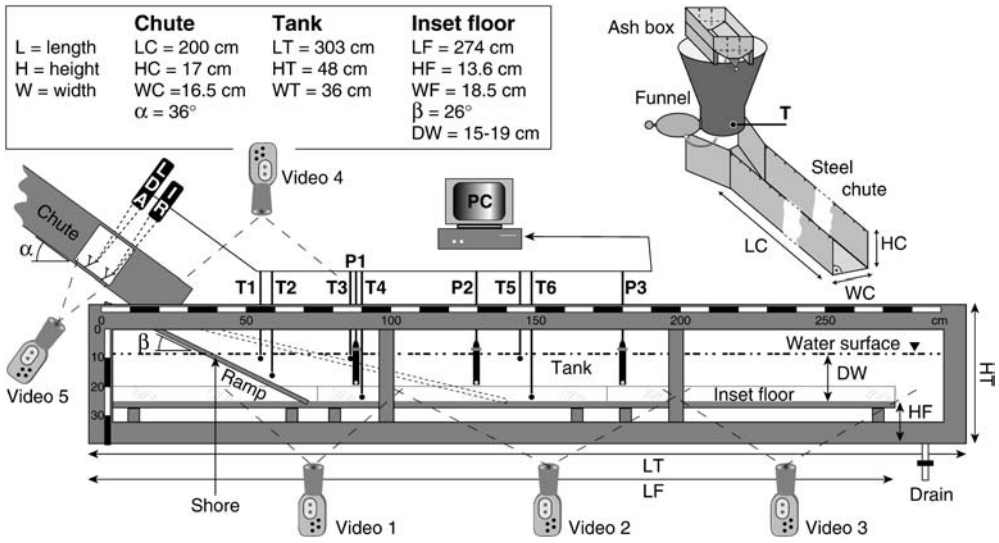

Fig. 2 Experimental setup showing arrangements in the tank of inset floor segments, sensors (*T* thermocouple, *P* pressure sensor, *IR* infra-red temperature sensor, *LDA* laser velocity meter), and camera views. *Top right* shows ash infill system and chute at smaller scale. Dimensions are given in the box. The *scale* on the tank is seen in video prints of Figs. 3 and 6, but data in the other diagrams are shown in terms of distance from shore

36°. The resulting rapid grain flows reached velocities of 1.5–2.5 m s^{-1}, measured by laser-Doppler anemometry (LDA in Fig. 2) near the end of the chute, where ash temperature recorded at 50 Hz by an infrared (IR) sensor showed negligible cooling during flow down the chute. The grain flows entered the tank and hit the shoreline on a ramp inclined at 26°, which continued into water and terminated on a horizontal plastic floor that extended down the tank. This inset floor was lined by 5.5-cm-high Perspex walls, had an inner width of 18.5 cm, and was elevated 14 cm above the tank floor and terminated 20 cm before tank end in order to avoid reflection of gravity currents, which instead dove and returned underneath the inset floor.

Thermocouples arranged along the floor and just below the water surface recorded temperatures in the tank at 20 Hz while three submerged pressure sensors recorded pressure fluctuations at 50 Hz (Fig. 2). Video cameras (25 fps) documented processes in the proximal, medial, and distal regions of the tank viewed from the side, proximal littoral interactions from above, and the grain flow through a glass window in the side of the steel chute. The inset floor consisted of segments that could be taken out to inspect and sample the sediments after the water had been carefully drained from the tank. Bottom sediment samples were taken as 2-cm-wide cut-outs across the width of the floor at locations chosen according to sediment distribution. Sample containers hung into the steel chute and either floating on Styrofoam rafts or mounted on the tank walls were used to collect sediment from ash clouds.

The ash used is from phonolitic ignimbrite T1 at Laacher See Volcano (Freundt and Schmincke 1986) with grains >4 mm sieved off, giving Md_Φ=2.5 and σ_Φ=3. The mean solids density is 1,910 kg m^{-1}, the loose-packed bulk density is 960 kg m^{-1}; lithologic components include slate, sandstone, and basalt lithics, crystals, and the coarsest pumice has a bulk density of around 500 kg m^{-1}. The effective friction angle of the loose-packed ash is 27°, measured where a 2.3-cm-thick ash layer of 414 cm^3 volume started to flow as the inclination of a steel plane was slowly increased. This friction angle allowed for rapid flow on the 36°-chute and there was no obvious change in behavior of the granular flows as they passed over the <20-cm-long ramp segment inclined at 26° before hitting the shoreline.

In the experiments reported here, ash mass (2.5–7 kg), ash temperature (61–403 °C), and water depth (4–19 cm) above the inset floor were varied. Run conditions for the experiments are compiled in Table 1.

Table 1 Experimental parameters. *T* Ash temperature; *m* ash mass; *t* duration; *M* mass flux of grain flow; *D* water depth to inset floor. Ramp inclination 26°, chute inclination 36°

Exp. no.	T (°C)	*m* (kg)	*t* (s)	*M* (g/s)	*D* (cm)
1	61	4.95	4.3	1,151	19
2	80	3.97	3	1,346	19
3	100	4.39	2.6	1,688	15
4	124	4.93	3.3	1,489	14.9
5	134	3	3.2	926	15
6	123	3.3	3.3	997	16
7	255	4.6	3.3	1,394	16.6
8	340	4.75	2.4	1,971	17
9	327	4.7	2.2	2,146	16.7
10	300	4.7	2.5	1,880	16.7
11	290	4.7	2.6	1,843	16.9
12	208	4.4	3.5	1,275	16.7
13	145	4.75	3.3	1,457	16.7
14	100	4	4	1,013	16.3
15	350	4.7	3.6	1,320	16.8
16	403	4.7	3.2	1,469	16.7
17	355	2.5	2.1	1,174	17
18	338	7	3.2	2,174	16.9
19	249	7	4	1,750	8
20	249	7	4	1,750	4.2
21	247	7	3.6	1,944	16
22	55	5	3	1,667	8

Table 2 Scaling of the experiments. q Volume flux per unit width; H thickness; L length; U velocity; γ strain rate of pyroclastic flow; D water depth; c shallow water wave speed; t_c = L/c characteristic time; d mean particle diameter; ρ_s = solids density; C solids volume fraction; C_{max} solids fraction at close packing; ρ_g density; η_g viscosity of dusty gas; k permeability; Δ gas diffusivity; Fr^* Froude number; q^* dimensionless flux

Pyroclastic flow properties				Pyroclastic flow scaling parameters		Experimental scaling parameters	
	From	To		From	To	From	To
q (m^2 s^{-1})	1	1,000	H/L	ca. 1×10^{-3}		1×10^{-3}	4×10^{-3}
H (m)	1	10	H/D	0.02	0.07	0.05	0.6
L (m)	1,000	10,000	D/L	2×10^{-2}	5×10^{-2}	2×10^{-3}	5×10^{-2}
U (m s^{-1})	30	150	N_S	2×10^{-6}	2×10^{-5}	7×10^{-4}	4×10^{-2}
γ (1 s^{-1})	30	15	N_B	1,970	2,260	950	3,920
D (m)	50	150	N_F	7×10^{-6}	8×10^{-5}	6×10^{-4}	1×10^{-3}
c (m s^{-1})	22	38	N_R	7×10^{9}	8×10^{10}	4×10^{6}	2×10^{7}
t_c (s)	45	26	N_P	0.101	0.003	6	100
d (m)	0.0005	0.001	t/t_c	0.3	0.7	0.3	0.8
ρ_s (kg m^{-3})	2,000		Fr*	1.4	3.9	1.2	3.6
C	0.4		q^*	0.04	2.6	0.04	0.57
C_{max}	0.6						
ρ_g (kg m^{-3})	2						
η_g (Pas)	2×10^{-5}						
k (m^2)	1×10^{-11}						
Δ (m^2 s^{-1})	0.01						

Scaling

The grain flows were variably unsteady because the ash did not collapse steadily from the funnel. Flow durations varied from 2 to 4 s, resulting in time-averaged mass fluxes of 0.9 to 2.2 kg s^{-1}. Rapid grain flow motion was dominantly saltational; sliding was only observed in their waning stage. The concentrated flow body was generally <3 cm thick, but saltating grains reached 5 cm above the chute floor. A short, dilute flow head of saltating grains was 4–5 cm deep. A dilute fine-ash cloud accompanied the grain flows down the chute. Because loose-packed bulk density of the ash was less then the density of water, so was the grain flow bulk density. I employ dimensionless parameters developed and reviewed by Iverson and Denlinger (2001) in order to check if the experimental flows adequately scale to natural flows (Table 2).

Geometric aspect ratios are H/L of height to length of a pyroclastic flow, H/D of flow height to water depth, and D/L of water depth to flow length; experimental values of flow length L were determined as the product of observed flow velocity, U, and duration, t. The number N_S relates grain collisional to friction-producing gravitational stresses; values $N_S<<0.1$ characterize friction-dominated flows. The Bagnold number N_B relates granular to viscous stresses, where granular stresses dominate at values $N_B>450$ because gas viscosity is so low. The number N_R is analogous to the Reynolds number in Newtonian flows and large values indicate insignificance of viscous effects. The fluidization number N_F is the ratio of fluidizing gas flux to solids velocity, where motion of gas relative to solids is sufficiently low at values $N_F<<1$ that mixture density remains constant. The number N_P is the ratio of timescales for downstream flow and upward pore-pressure diffusion. Pore pressure may persist during flow runout when $N_P<<1$.

Scaling the relation of a pyroclastic flow to the water body is largely based on the speed of shallow-water waves, $c=(gD)^{1/2}$, where g is acceleration due to gravity and D is water depth. The ratio t/t_c relates the duration, t, of pyroclastic flows to the characteristic time for the propagation of disturbances in the water, $t_c=L/c$ (Tinti et al. 2001). The Froude number Fr*=U/c characterizes the tsunami-forming potential of the flows (Tinti et al. 2001). The volume flux per unit width, q, of a pyroclastic flow is compared with the limiting flux of water displacement, cD, by the ratio $q^*=q/cD$, which strongly controls wave amplitude (Walder et al. 2001). In the experiments, only the time-averaged rather than the dynamically more significant peak values of q (cf. Walder et al. 2001) could be determined.

Data in Table 2 show that experimental and natural flows agree well in the geometric ratios H/L, H/D, and D/L, in the numbers N_S, N_B, N_F, and N_R characterizing grain flow behavior, and in the time ratio t/t_c and the Froude number Fr* related to the interaction with the water body. Major differences between experiment and nature occur in the number N_P and the dimensionless flux q^*. Values $N_P>1$ in experimental flows indicate these were unable to build up any significant pore pressure in contrast to natural flows that extend to values $N_P<<1$ due to their much greater thickness. Experimental values of $q^*<0.6$ straddle the lower end of the range for natural flows, which extends to $q^*>2$ (Table 2). Implications of these limitations will be discussed later. Thermal interactions in experiment and nature should be similar since the same thermodynamic properties of ash and water are involved, but natural ash temperatures can be higher than those used in the experiments and high natural mass fluxes may facilitate development of higher steam pressures as in the experiments; these aspects are also discussed later.

In the following, the interaction phenomena during entry of the experimental pyroclastic flows into water that

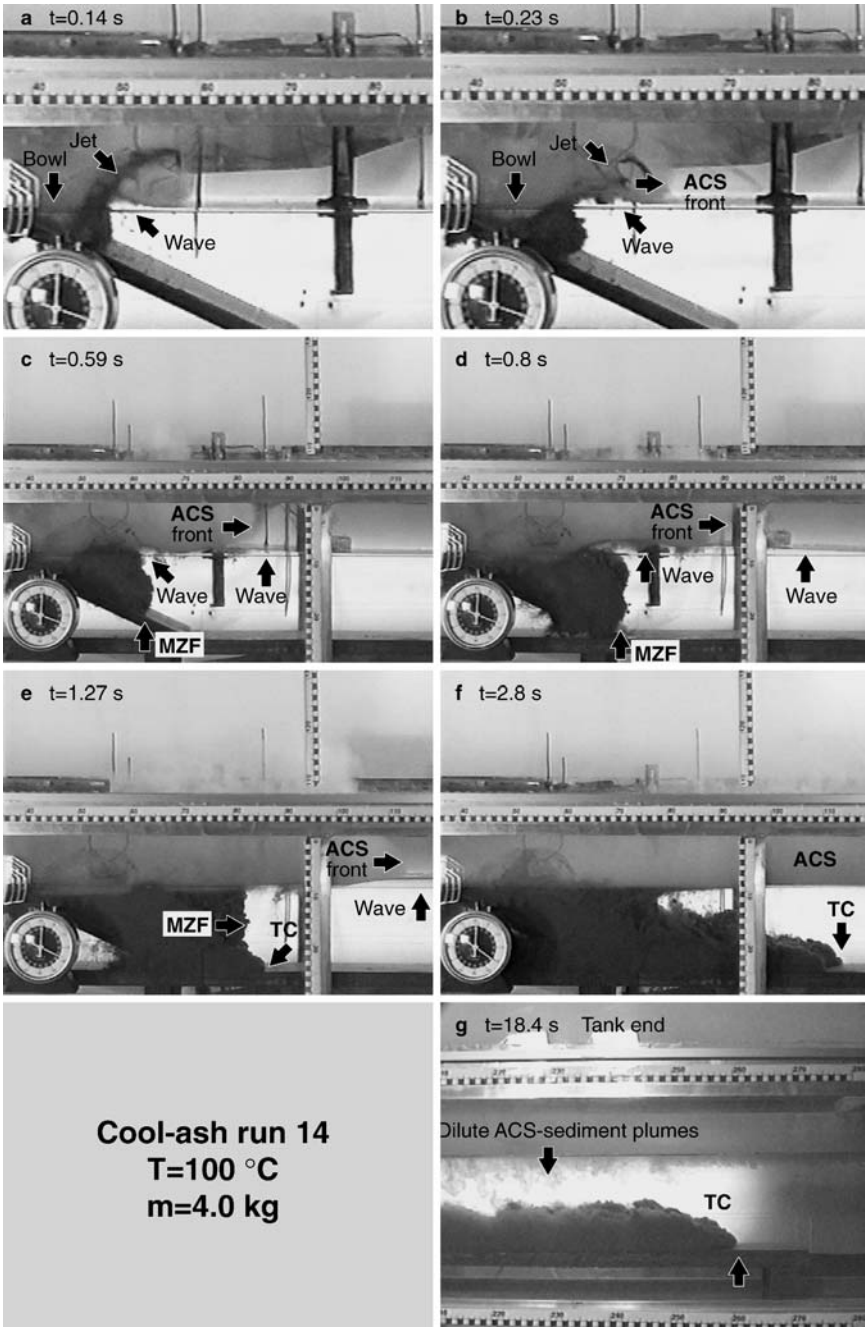

Fig. 3 Video prints of Exp. 14 (Table 1) showing the first few seconds of entry of a cool pyroclastic flow, and the distal turbidity current at a late stage in **g**. Note larger scales in **a** and **b**. *Scales* on tank have centimeter divisions. *ACS* Ash-cloud surge over water; *bowl* depression in water surface at shore; *MZF* steep front of mixing zone; *TC* turbidity current. A video of this run is available as Electronic Supplementary material

are separate for relatively cool flows (<150 °C) and relatively hot flows (>250 °C) are described, but flows at intermediate temperatures show transitional behavior.

Observed interactions

Entry of cool pyroclastic flows

Video prints of an experiment with T=100 °C (Exp. 14, Table 1) are shown in Fig. 3. When the grain flow front hit the shoreline, water was pushed out of a bowl-shaped littoral depression and formed a wave composed of a leading high-amplitude bulge and a trailing low-amplitude trough (Fig. 3). The wave escaped from the nearshore region at increasing speed (Fig. 4a, b). Initially, part of the grain flow jetted up the upstream-facing wave flank much like it were a solid surface, rapidly decelerated from the incoming grain flow velocity (Fig. 4a), and then dropped back onto the water and mixed with it (Fig. 3a, b). Grain flow material arrived continuously after the initial splashing entered the water without forming further ash jets, but additional waves were generated when particularly strong pulses of higher mass flux arrived. After initial splashing, two phenomena happened simultaneously.

Most of the material penetrated the water surface and formed a turbulent mixing zone in the water that had a nearly vertical interface to clear water and gradually this extended downstream to reach an approximately constant position when the incoming grain flow waned (MZF in Figs. 3c, d, and 4a, b). Because the granular flow of this run consisted of discrete pulses, several waves formed in rapid succession during the mixing process and partly united as they moved down the tank (Fig. 4b); the first wave generated upon grain-flow entry usually had the highest amplitude. A significant fraction of vesicular pumice lapilli separated buoyantly during the mixing process to form extensive pumice rafts floating on the water surface, while coarse and dense material rapidly sedimented along the base of the mixing zone. The head of a turbidity current emanated from the base of the mixing zone front (Fig. 3e–g) where it stopped to expand (Fig. 4b). The turbidity current released additional buoyant pumice swarms and gradually decelerated (Fig. 4c) as it advanced down the tank along the floor.

The second phenomenon, operating simultaneously, was the formation of an ash-cloud surge (ACS) that was optically much denser than the ash cloud accompanying grain flow down the chute (Fig. 5). The ACS formed where the grain flow hit the water surface (Fig. 3); initially it had a high velocity (Fig. 4a), but gradually decelerated as it traveled down-tank over the water (Fig. 4c). ACS-formation continued as long as the granular flow was maintained. Sediment falling from the ash-cloud surges created dilute, slowly sinking plumes of fine ash in the water (Fig. 3g).

When the incoming pyroclastic flows terminated, water flushed back to the original shoreline, the mixing zone gradually collapsed, and the turbidity current drained off, leaving turbid water in the tank.

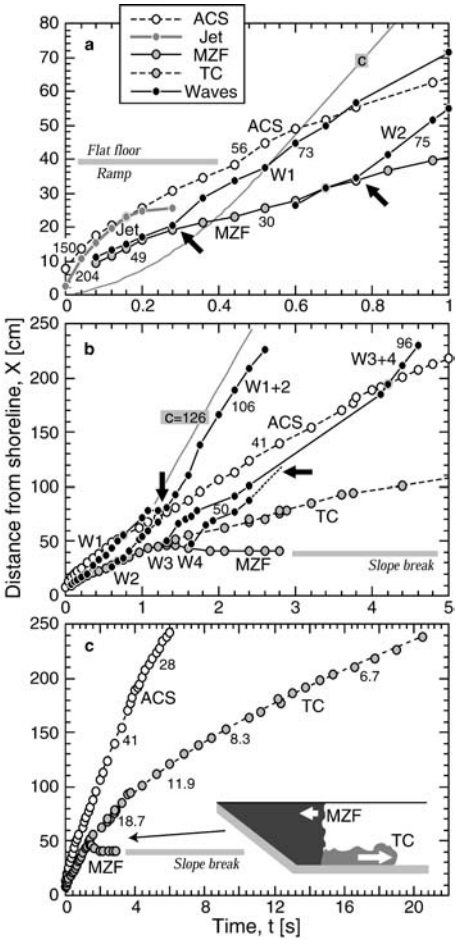

Fig. 4 Position of flow fronts and wave crests over time in cool-ash run 14 (Table 1) as measured from video records. **a–c** Different time windows for clarity. *W1–W4* Subsequent waves, which unite downstream to *W1+2* and *W3+4* (at *arrows* in **b**). Waves *W1* and *W2* detach from mixing-zone front at *arrows* in **a**. Curve c shows (in **a**,**b**) the calculated positions for a shallow-water wave originating at x=0 and t=0 for comparison. *Small numbers* indicate local velocities (cm s^{-1}). Minor scatter in the data is due to combining three video records from different viewpoints and from perspective distortion away from the center of the field of view in each. *Inset* in **c** illustrates turbidity current emerging from mixing zone

Entry of hot pyroclastic flows

A time sequence of video prints from a representative hot-ash experiment (T=350 °C, Exp. 15, Table 1) is shown in Fig. 6. Ash-cloud surges overriding hot grain flows on the chute were optically denser and of greater depth than those associated with cool flows. The initial moment of entry of the flow front into the water was similar as with cool flows: a wave formed from water displaced from shore, an initial ash jet surged over water, and an ash-cloud surge optically denser than the one along the chute was generated while coarser ash mixed into the water (Fig. 6a). Shortly after the onset of mixing, however, steam explosions began (Fig. 6b), which generated a rumbling noise and consisted of back-dropping ash fountains and a fine-ash plume rising by thermal convection up to the ceiling of the lab and emplacing fallout ash outside the tank. The underwater mixing zone then did not extend down the ramp as in cool-ash runs, but rather along the water surface (compare Fig. 6b–d with 3c–e). The finer-grained load of the ash fountains contributed to the ash-cloud surge while coarser sediment mixed with the water to form dense sinking sediment plumes from which the coarsest particles rapidly fell to the floor (Fig. 6c, d). Further explosions were generated from this along-surface mixing zone, with fountains throwing ash farther downstream (Fig. 6d). These subsequent explosions were often more vigorous than the initial explosion close to shore. The distance from shore across which the steam explosions occurred extended as long as the pyroclastic flow was maintained.

The ash-cloud surge generated through the steam explosions, and the sediment plumes falling from it through the water, were much denser than in cool-ash runs (compare Fig. 6g with 3g). The ACS initially decelerated away from shore, but strong explosion pulses formed denser and faster ACS-pulses propagating to the

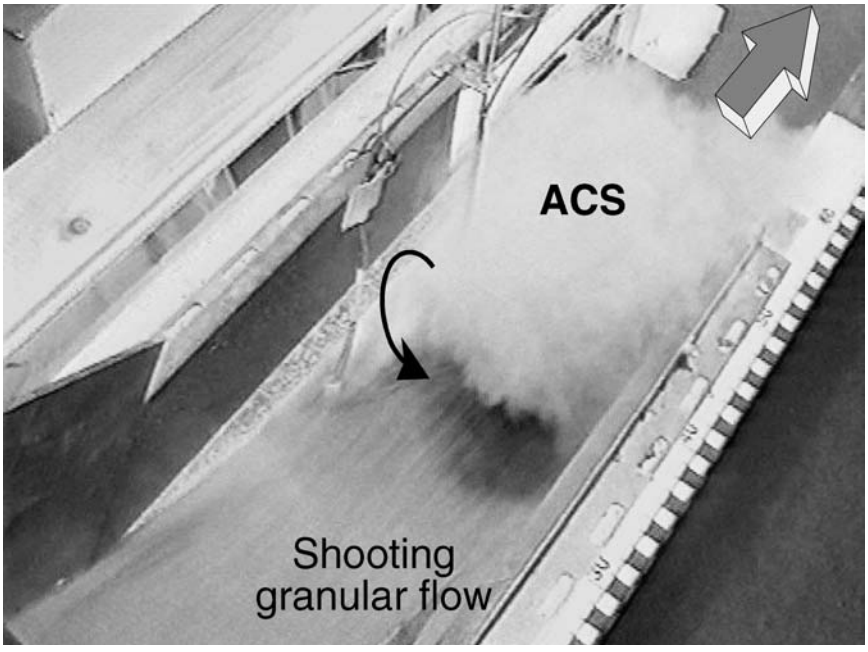

Fig. 5 Ash-cloud surge formation upon entry of a cool pyroclastic flow seen from above (Exp. 5, Table 1). The very faint ash cloud atop the grain flow allowed observation of ACS-formation at the shore

front of the ACS, which then accelerated (see ACS-front speed increasing from 48 to 113 cm s^{-1} after explosion started at around t=0.8 s in Fig. 7b). Strong explosion pulses also generated water waves, such as wave 2 in Figs. 6b and 7a, b, which often had a greater amplitude than the wave generated upon initial impact. The waves remained slower than expected within the range of ash-fountaining and only reached their equilibrium shallow-water-wave velocity farther downstream (at >100 cm from shore in Fig. 7b). The tip of the underwater sediment-plume region (SPT in Figs. 6 and 7) approximately marked the downstream fountain edge and trailed the explosion-generated wave (Fig. 7a, b) as long as the region of explosions extended away from shore. Within this range, the underwater sediment plumes were apparently largely composed of ash-fountain sediment (Fig. 6d), but beyond this range they were composed of sediment falling out of the ash-cloud surge (Fig. 6f) and the SPT thus trailed the ACS, but increasingly lagged behind as ACS fallout waned (Fig. 7b).

The base of the underwater mixing zone (MZB in Figs. 6 and 7) advanced along the floor much more slowly than the tip of the sediment-plume region (SPT) because material transport was dominantly along the surface. Sinking sediment plumes touched the floor and dropped their coarser load while finer material remained in suspension and generated a turbidity current. Further sediment plumes added to the top and to the head of the turbidity current or touched down in front and merged with it, causing jumps in the position of the turbidity-current front (Fig. 7b). Turbidity currents in hot-ash runs thus formed progressively by collection of falling sediment plumes over some length of the tank; in contrast, they formed from a confined mixing zone close to the shore in cool-ash runs. Added sediment plumes became more dilute downstream (Fig. 6g) and had a waning effect on the turbidity current.

A combination of phenomena observed in cool and hot experiments occurred in a run using an intermediate ash temperature of T=208 °C (Exp. 12, Table 1). The granular flow initially entered the water as in a cool-ash run, producing a wave, an ash-cloud surge, and a steeply bounded underwater mixing zone from which a turbidity current began to emerge. Explosions started from the top of the mixing zone after about 1 s, threw ash forward onto the water surface generating sediment plumes merging with the turbidity current, generated a new wave and added to the ash-cloud surge, which subsequently briefly accelerated. This ash-cloud surge did not reach the tank end, but stopped on the way and lofted as a dilute ash plume.

Using shallower water depths in hot-ash experiments of the same temperature (cf. Exps. 19–21, Table 1) had the main effect that steam explosions extended farther downstream, wet ash was ejected higher above the water, and ash fountains were even more strongly forward directed. Due to the shallow water depths (D=4–8 cm), almost total ash transport across water, and massive deposition from ash fountains into water, a turbidity current did not develop within the length of the tank.

Deposits under and over water

Underwater deposits

In cool-ash runs, mixing with water sometimes remained incomplete and pockets of air became trapped in the deposit, which subsequently escaped upwards, disturbing the deposit by partial turnover, releasing buoyant pumice

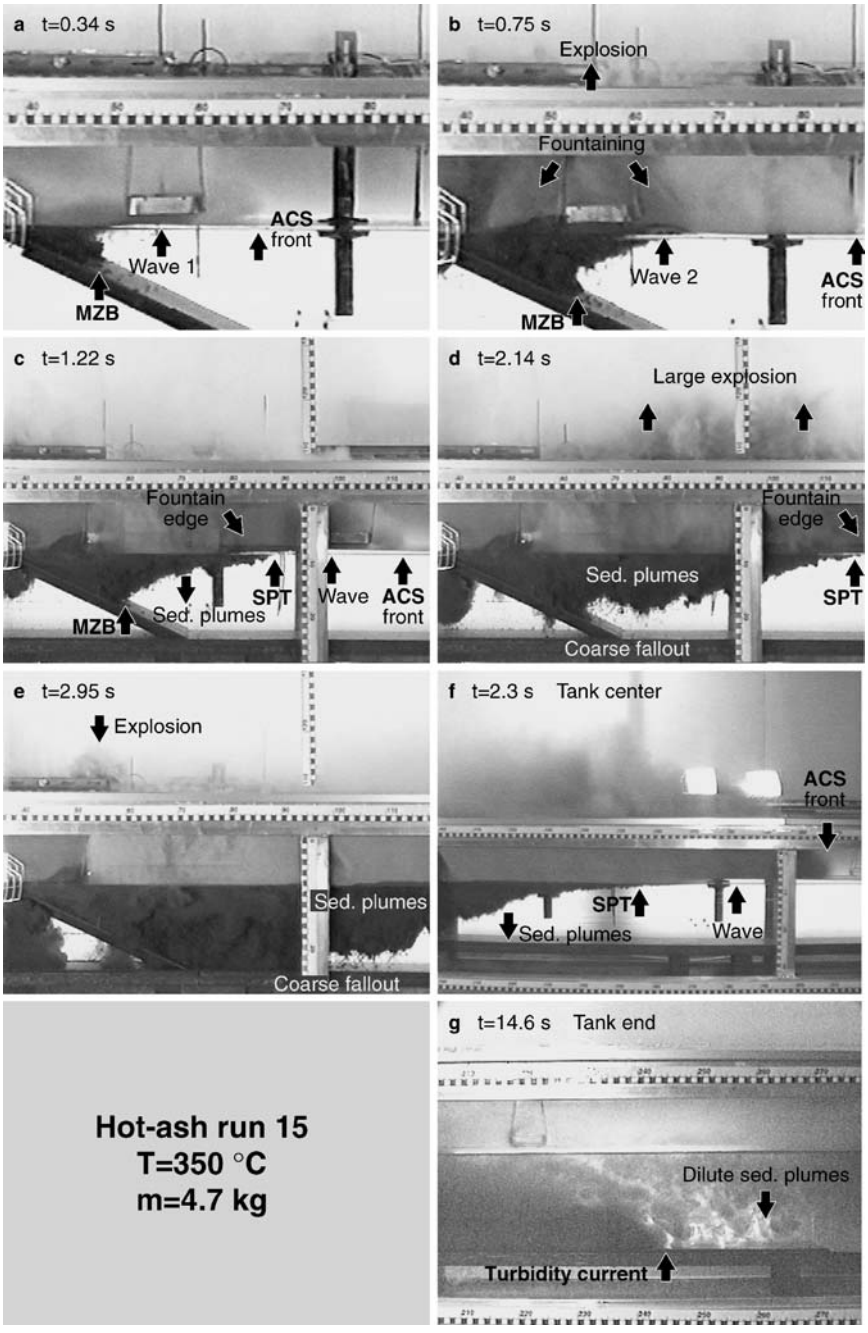

Fig. 6 Video prints of hot-ash run 15 (Table 1) showing the first few seconds of entry and the distal turbidity current advancing through sinking ACS-derived sediment plumes in **g**. Note larger scales in **a** and **b**. Note also how sites of distinct explosions vary between **b**, **d**, and **e**, the one farther out in **d** being the most vigorous. *SPT* marks the tip of the underwater sediment-plume region, *MZB* the basal front of the mixing zone. Coarse fallout from sediment plumes is seen in **d**, **e**. A video of this run is available as Electronic Supplementary material

lapilli and turbid ash plumes to the overlying water, and triggering local downslope sediment slumping and small secondary turbidity currents. In all cool-ash runs, much of the rapidly accumulating sediment underneath the mixing zone slumped down the 26° ramp during or shortly after deposition. Maximum sediment concentration therefore, occurred at the base of the ramp, followed by an exponential downstream decay of a deposit laid down by a progressively diluting turbidity current (Fig. 8a). McLeod et al. (1999) also observed maxima in sediment concentration near the ramp base in high-particle-concentration liquid density currents, which they attributed to the opposing influences of downstream variations in velocity and particle content of the flows; here such maxima were clearly controlled by slumping. The proximal slumped deposit was normally graded through ungraded, occasionally contained internal unconformities and local crude cross stratification, and had an irregular, wavy, or lobate surface. The flat-topped turbidity-current deposit was normally graded and systematically finer grained downstream. The entire subaqueous deposit was capped by a very thin top layer of fine ash that had settled from the turbid water and became overlain by pumice lapilli that ultimately soaked and sunk from the pumice rafts at the water surface.

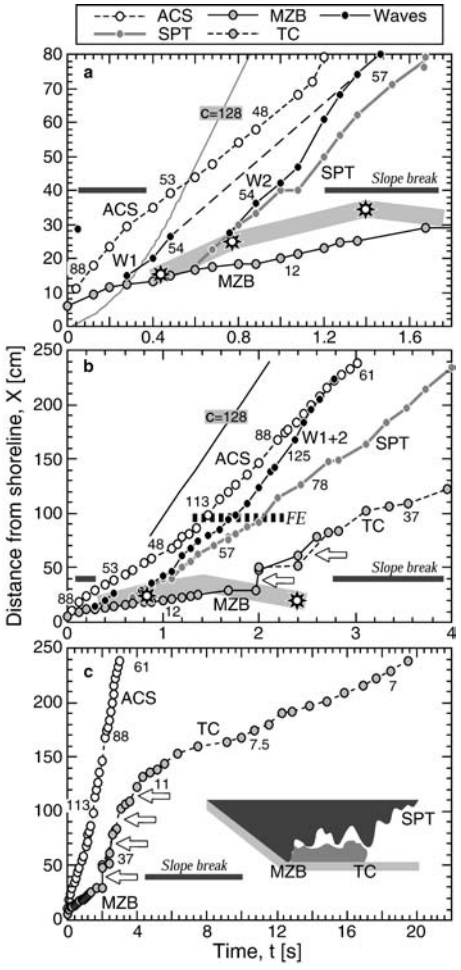

Fig. 7 Position of flow fronts and wave crests over time in hot-ash run 15 (Table 1). **a–c** Different time windows for clarity. *Bold gray line* indicates region of steam explosions, *stars* mark the strongest events seen on video. *Dashed bar* (*FE*) in **b** shows maximum fountain edge position beyond which wave detaches from SPT. *White arrows* in **b**, **c** indicate sediment-plume additions to turbidity current as illustrated in the *inset*

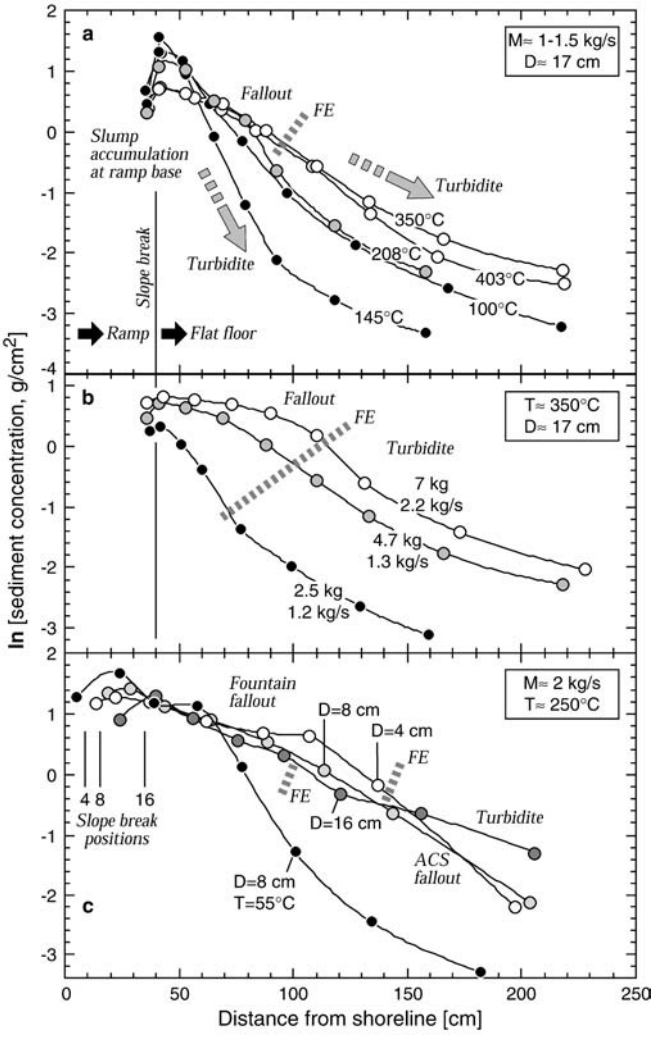

Fig. 8 Sediment concentrations of deposits along tank floor for experiments using different **a** ash temperatures, **b** ash masses, with estimated time-average mass fluxes given, and **c** water depths. *Dashed bars* (*FE*) indicate maximum distance of fountain edge. **a** Turbidite deposits immediately follow proximal slumps in cool-ash runs, but only dominate behind the fountain edge in hot-ash runs. **b** Sediment is progressively displaced downstream at higher ash masses. **c** Sediment distribution is similar for hot-ash runs in 4–16-cm deep water although transport mechanisms were different: mainly turbidity current at D=16 cm, but fallout at D=4–8 cm. Position of slope break lies closer to shore at shallower water depth. Data from a cool-ash run (*black dots*) given for comparison

In hot-ash runs, sediment slumping down the ramp occurred mainly after the entry of hot granular flows was over. Maxima of sediment concentration at the base of the ramp were less pronounced than in cool-ash runs (Fig. 8a) because most ash was initially transported along the water surface at high temperatures. The deposit on, and immediately below, the ramp had a lobate surface, was normally-graded, but poorly sorted, and occasionally was crudely bedded, contained pumice- or lithic-enriched flat lenses or a lithic lag-breccia formed on the upper ramp. On the flat floor, the deposit was divided into a coarse-grained, variably fines-depleted and normally graded lower layer overlain by a finer-grained, more poorly sorted normally graded upper layer. The lower layer was mainly responsible for the wavy surface morphology of the deposit across medial distances by forming coarse-grained mounts above which the upper layer was thinner. The lower layer was largely composed of the coarser material that fell from sinking sediment plumes, forming mounts where local sedimentation rates were particularly high (cf. Fig. 6d, e), whereas the upper layer was deposited by the turbidity current.

Over some proximal distance, up to where the fountain edge (FE in Fig. 8a) reached, deposit concentration decayed only gradually followed by an exponential decay downstream of the fountain edge; the lower layer thinned more rapidly than the upper layer. Underwater sediment was distributed farther downstream in hot-ash runs compared with cool-ash runs of comparable initial mass flux (Fig. 8a, c), due to the enhanced and faster transport along the water surface. The downstream displacement of

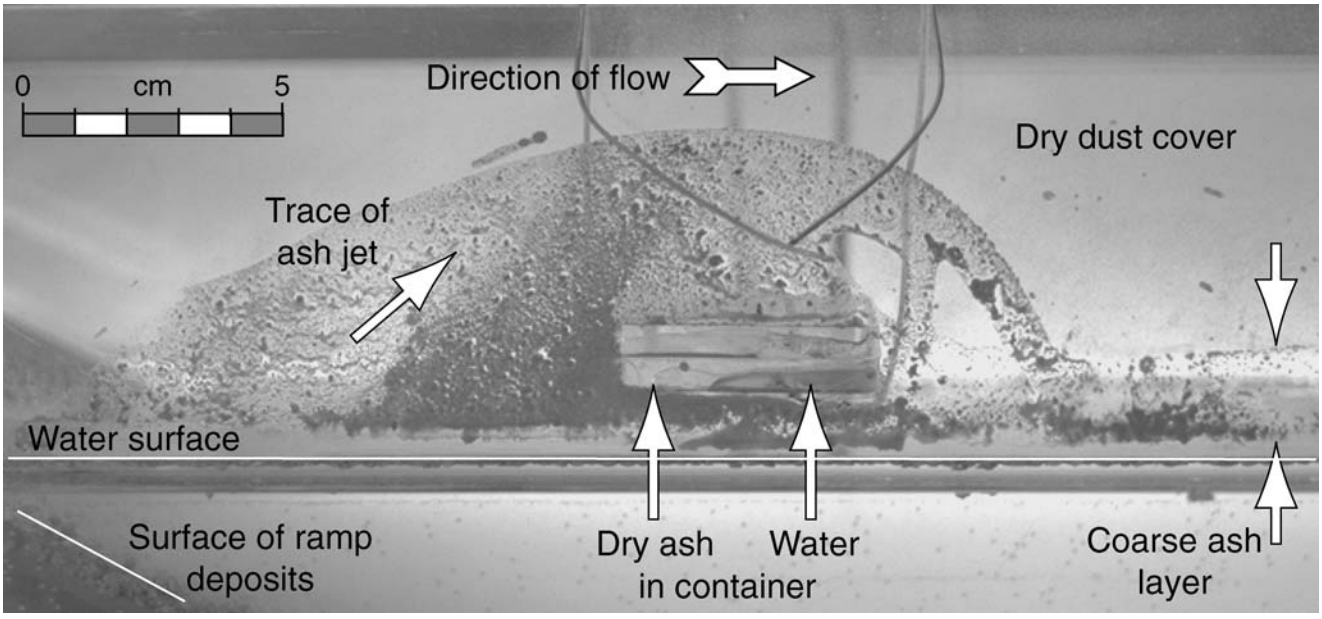

Fig. 9 Sediment trace of a wet ash jet on the pane, cool-ash run 14. The jet splashed across the sample container into which dry ash and water were deposited. Fine dust from the ACS covers the pane around and behind the jet trace except for a 2–3-cm-thick basal layer of coarser ash where the pane had been wetted by a preceding wave

the sediment mass increased with initial mass or mass flux of the incoming ash at the same temperature (Fig. 8b), reflecting the farther downstream range of explosions combined with greater sedimentation rates from the subsequent ash-cloud surge. Other conditions constant, decreasing the water depth from 16 through 8 to 4 cm did not significantly affect the downstream sediment distribution at high ash temperature although the emplacement mechanisms were different (Fig. 8c). A turbidity current formed at D=16 cm, but not at the shallower water depths, where floor sediments were emplaced by fallout from the ash fountains and ash-cloud surges. A turbidity current did develop, however, at D=8 cm using cool ash (Fig. 8c).

All floor deposits of hot-ash runs were covered from proximal to distal sites by a thin (1–2 mm) layer of massive very-fine ash that had settled from the turbid water; it also covered all pumice present at the deposit surface that had settled quickly. In contrast to extensive pumice rafts formed in the cool-ash runs, virtually no floating pumice was observed when ash temperatures exceeded about 250 °C. Whitham and Sparks (1986) also observed hot (>200 °C) pumice of around 500 kg m^{-3} bulk density to sink in water and they explained this phenomenon by conversion of adsorbed water to steam, which flushes air out of the pore space, followed by condensation during subsequent cooling and rapid suction of water into the pumice.

Over-water ash-fountain and ACS deposits

In cool-ash runs, ash-cloud surge deposits collected in containers mounted on the side walls of the chute and above the water surface in the tank were dry, massive, but very thin (<1 mm), and composed of fine ash. Layer thickness across the containers, rectangular boxes with 14-mm-high walls, was constant. Stereo-microscopic inspection showed that the deposits formed a highly fragile, extremely porous "dendritic" framework of stacked ash particles, reminiscent of a reticulate structure, which was easily compacted by shaking. Thickness and structure suggest gentle fallout deposition although the ash was deposited from laterally flowing turbulent ash-cloud surges. The ash-cloud surges left a thin cover of ash on the glass panes above the water surface, except for the lowermost 1–2 cm where ash was washed off by reflected waves late in the experiments. This ash cover was sharply divided into a lower wavy, ca. 2-cm-thick layer of coarser, poorly sorted ash that ranged from close to the shore almost up to where the underwater mixing zone extended, sticking to the panes where these had been wetted by the preceding waves, and an upper layer of fine dust sticking to the panes where they had remained dry. Because the waves traveled to the end of the tank, but the coarser ACS sediment terminated near the maximum extent of the mixing zone, the ash-cloud surges had apparently lost such load at this distance. Whether the ash transported in the lower ca. 2 cm of the ash-cloud surges was dry (and only wetted upon contact with the panes), or already wet during transport, is not known. Close to the shore, the lower ash layer merged into a thicker bulge of ash on the panes that marked the passage of the ash jet (see Fig. 3a, b). The trace of an exceptionally well-developed jet is shown in Fig. 9. The Perspex container overwhelmed by this jet contained a small puddle of water next to the dry ash, showing that both ash and water

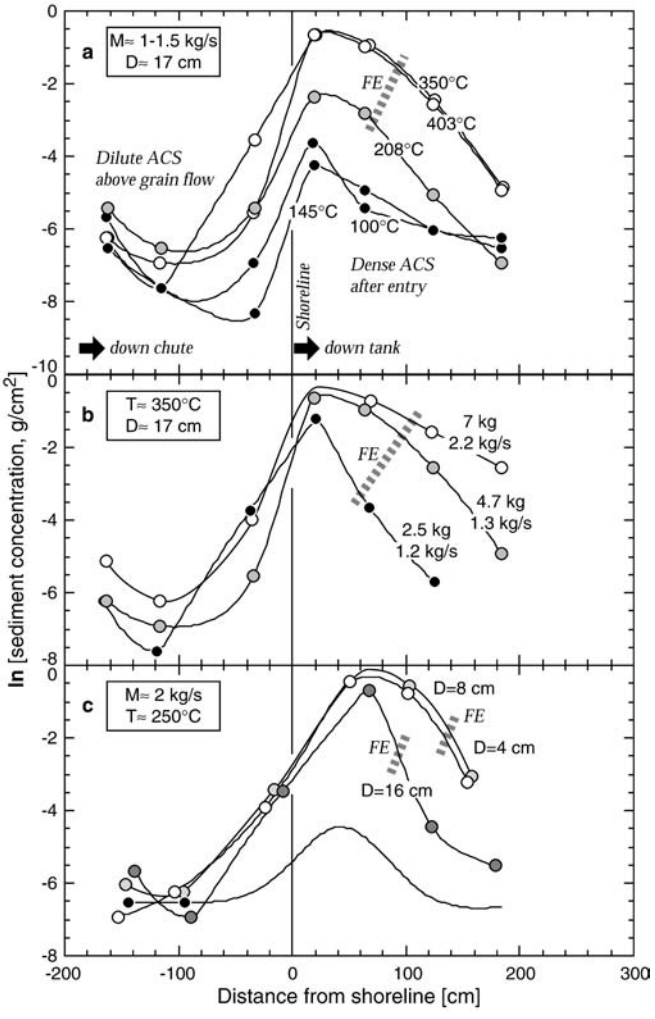

Fig. 10 Ash-cloud surge (ACS) sediment concentration along the chute and tank for experiments using different **a** ash temperatures, **b** ash masses, with mean mass fluxes indicated, and **c** water depths. A 3–4-ln unit jump across the shoreline equal to a 8–16 times increase in sediment concentration implies a similar magnitude of increase in particle concentration in the ash-cloud surge. *Dashed bars* (*FE*) indicate maximum fountain-edge position

were ejected in the jet, but mixing remained incomplete that early in the interaction.

The ash-cloud surge deposit concentration in cool-ash runs is low along the chute, but suddenly jumps to much higher values beyond the shoreline (Fig. 10a). Assuming the same emplacement times for all sample containers (which cannot be precisely determined, but must have varied by less than a factor of 2), sediment concentration is proportional to sedimentation rate, which in turn is proportional to particle concentration in a dilute suspension current when current velocity does not change much (cf. Freundt 1999). The upward jump in ACS-sediment concentration for the cool-ash (100–145 °C) runs in Fig. 10a thus suggests 8–16 times increase in ACS particle concentration, confirming the visual observation of a much higher density of ash-cloud surges formed by the interaction near shore (Fig. 5). Decreasing ACS particle content due to sedimentation during run-out down the tank then resulted in deposit concentrations decaying exponentially with distance (Fig. 10a).

Two layers can also be identified in the deposits on the panes of hot-ash runs (Fig. 11). A major difference to cool-ash experiments is that the coarser-grained, more poorly sorted lower layer (sticking where panes had been wetted by waves) mostly extended through the length of the tank, although sediment concentration and grain size gradually decreased. The transport capacity of ash-cloud surges thus was greater in hot than in cool-ash experiments. The thickness of vaguely through sharply bedded ash deposited into containers above the water increased against the downstream container walls (Fig. 12), showing that lateral flow strongly influenced deposition. This is also evident from wet ash that covered vertical metal rods (sensor supports) sticking out of the water in much greater thickness on the upstream-facing than on the downstream-facing side. Thick ash covers such as those seen in Fig. 11 certainly imply the ash was wet during emplacement (as opposed to dry ash sticking to a wetted surface) and, hence, an ash–water mixture was transported in the explosion fountains and possibly over some proximal distance in the lower ca. 2–3 cm of ash-cloud surges. Sensor supports in distal reaches of the tank, however, were evenly and thinly covered by fine ash, and thin layers of dry massive fine ash of constant thickness had been emplaced in the distal sample containers.

ACS-sediment concentrations in Fig. 10a show that, at higher ash temperatures, denser ash-cloud surges already developed as the pyroclastic flows moved down the chute; this is probably related to the heating and escape of admixed air. Yet even denser surges formed by the interaction with water behind the shore. The increase in ACS particle concentration near shore is of similar magnitude as in cool-ash experiments. Greater ACS sediment masses were emplaced farther from shore, and the region of exponential decay was correspondingly displaced downstream at higher temperatures (Fig. 10a, c), higher ash masses or mass fluxes (Fig. 10b), and lower water depths (Fig. 10c), because all these parameters favor greater intensity and downstream extent of steam explosion fountains feeding the ash-cloud surges. The exponential decay following the maximum in sediment concentration is steeper for the hot-ash runs, in which the ash-cloud surges contained more coarse-grained ash that sedimented at higher rates. Proximal sedimentation rates may also have been enhanced by aggregation of wet ash in the lower parts of the currents.

Proximal steam explosions ejected wet ash that stuck to the panes forming a thick bulge that merged with the lower layer farther downstream (Fig. 11). This explosion-derived deposit contained the coarsest wet ash, partly in the form of wet “mud balls” up to >1 cm in diameter, which also speckled the panes above the lower layer otherwise coated with dry ash. Sediment collected in containers 2–3 cm above water within the range of explosions was a wet mixture of poorly-sorted ash and mud-balls (Fig. 12a). Fallout on the tank rim ca. 20 cm

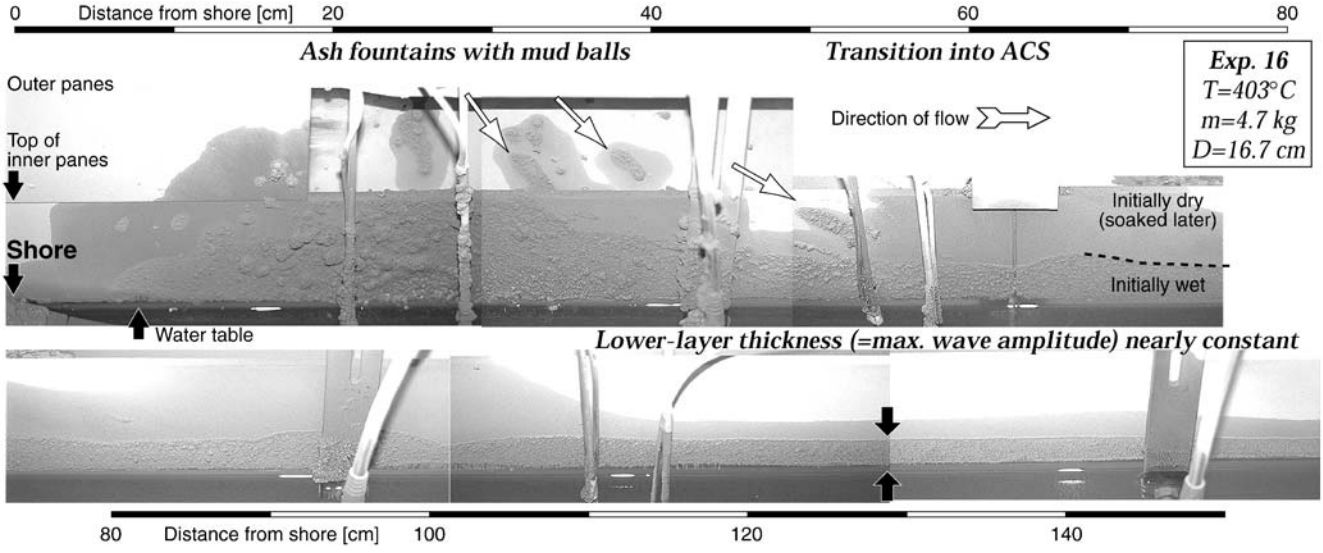

Fig. 11 Ash deposits on the panes above water from a hot-ash (403 °C) run 16 (Table 1). *Top*: near-shore interval of explosions and ash fountains with a transition to surge at right. Note sediment sticking to sensor rods and downstream decreasing angle of mud-ball trajectories (*arrows*). *Bottom*: wavy through planar boundary (i.e., trace of maximum wave crest) between upper dry fine-ash coating and lower layer of coarser ash (*between arrows*) sticking on wetted pane

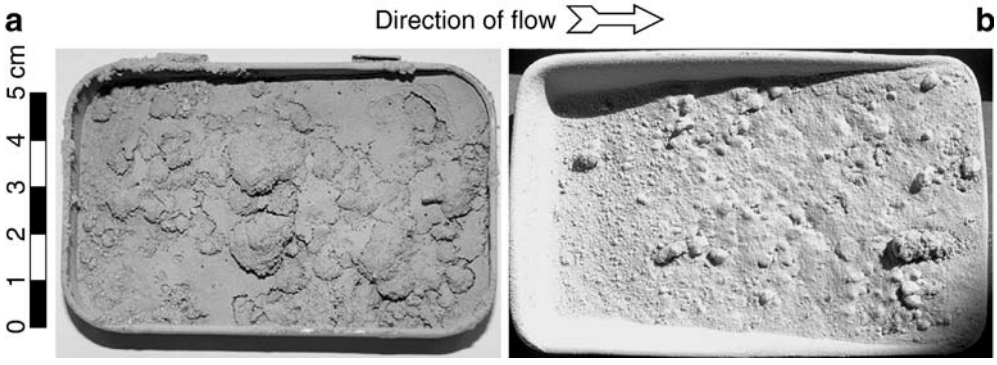

Fig. 12 **a** Ash deposit containing mud balls collected in a container above water at 20 cm from shore in Exp. 16 (cf. Fig. 11). **b** Deposit of ash-cloud surge collected 63 cm from shore in Exp. 10 (300 °C; Table 1). Deposit thickness increases in the direction of flow from left to right

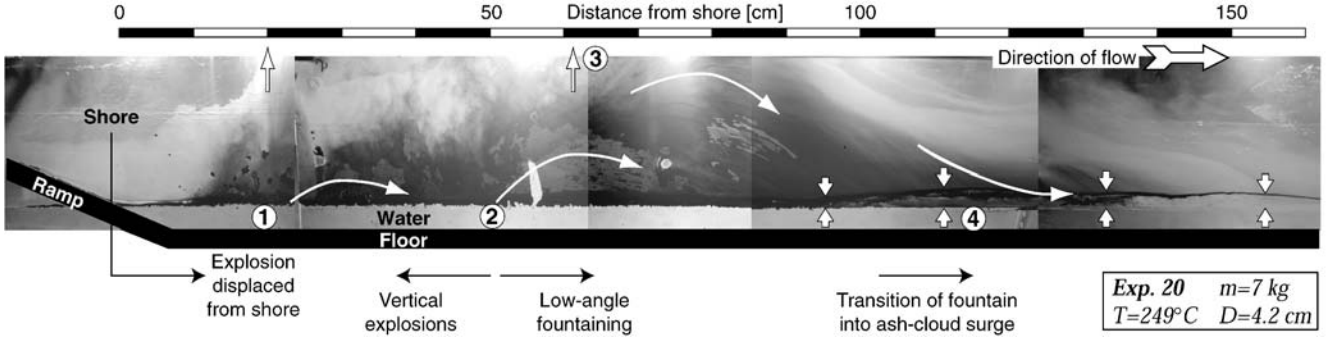

Fig. 13 Exceptionally well-preserved ash-fountain traces from run 20 (Table 1) using shallow water depth of 4 cm. *Points 1–4* are discussed in the text. Note low-angle fountain trajectories with transition to ash-cloud surge to the right

above water surface, emplaced by ash fountains that jetted out of the tank, was dry, moderately sorted ash, but also contained some moist spherical ash aggregates a few millimeters in diameter. Convectively rising plumes left well-sorted, dry fine ash on Perspex walls lining the tank-top. Ash traces of explosions were particularly well preserved on the panes in an experiment using shallow water (Fig. 13). In this run (Exp. 20, Table 1), the first explosions generated some 20 cm from shore (1 in Fig. 13), ejected mud balls ballistically and shot wet and

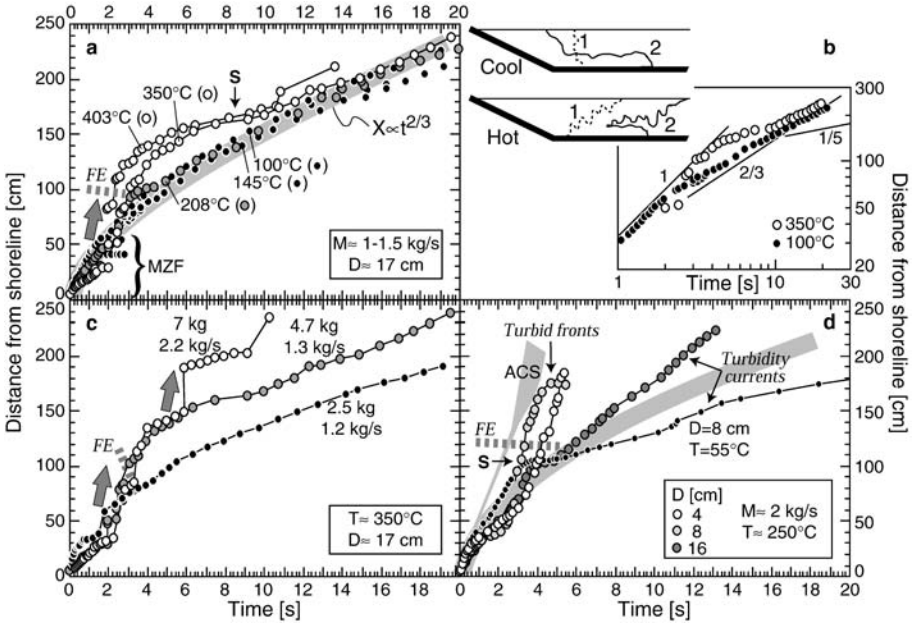

Fig. 14 Position of turbidity-current front over time for experiments using different **a** ash temperatures, **c** ash masses, and **d** water depths. *Dashed bars* (*FE*) indicate extent of fountain edges. **a** *S* marks near-stagnation of turbidity currents in hot-ash runs. **b** A log-log plot facilitates comparison of two data sets from **a** with lines of slope 1 ($x \propto t$), slope 2/3 ($x \propto t^{2/3}$, also shown as *bold gray line* in **a**), and slope 1/5 ($x \propto t^{1/5}$ for viscous flows) as discussed in the text. Schematics show different relations between mixing zones and turbidity currents at subsequent times 1 and 2. **d** Data for hot-ash runs at D=4–8 cm show advance of turbid fronts from fountain and ACS fallout; turbidity currents did not form in these runs. *Gray field* ACS shows ash-cloud surge advance from Fig. 15d for comparison with advance of turbid fronts at D=4–8 cm. *Bold gray line* represents cool-ash run data from **a** for comparison with cool-ash (55 °C) run at D=8 cm, in which the turbidity current briefly stopped at S and moved more slowly through the distal part of the tank

dry ash vertically upward, with the wet ash remaining limited to the lower 15–20 cm on the panes while dry ash covered the remaining height of the panes and was lifted high above the tank in a fine-ash plume. Such plumes contained visible steam, but steam condensation apparently did not affect ash transport and deposition under the laboratory conditions. Stronger explosions subsequently commenced some 50 cm from shore (2 in Fig. 13) generating low-angle ash fountains containing ash that was in part too wet to completely stick on the panes (light areas in Fig. 13). Ongoing explosions (3 in Fig. 13) produced an even stronger convective ash plume together with low-angle ash fountains reaching more than 20 cm above the water surface. The vertical ejection of wet ash was probably limited by efficient aggregation, which is prominently evident in the abundant mudballs. Downstream of the explosion site, the back-dropping fountains were horizontally deflected and part of the ash sunk into the water while the remaining part entered the ash-cloud surge. In this collapse region (4 in Fig. 13), the dark trace of the wave crest shows a significant increase in wave amplitude, suggesting that wave amplitude was enhanced by water displacement by massive ash deposition from the fountain.

Motion of flow phases

Mixing zones and turbidity currents

The steep front of the highly turbulent mixing zone in cool-ash runs advanced down tank at an approximately constant rate, which only decreased when the incoming granular flow waned, and ultimately retreated somewhat towards the shore when the input stopped. Highly unsteady mass flux of a granular flow, however, also caused unsteady advance of the mixing zone. The appearance of a turbidity current at the base of the mixing-zone front commonly correlated with the onset of decaying advance. This delay in turbidity current formation of about 1–3 s is interpreted as the time necessary to form a higher-concentration basal suspension by particle settling in the mixing zone facilitated by decreasing turbulence as the ash input waned. The turbidity currents in cool-ash runs decelerated from high initial velocities as they advanced down the tank floor through 17-cm-deep water (Fig. 14a) while overlying clear water moved back towards the shore. A turbidity current in 8-cm-water depth was initially faster than those in deeper water, but then stopped (at S in Fig. 14c) when overlying water strongly flowed back towards the shore; later it continued through the rest of the tank at lower speed than currents in deeper water. At comparable ash influx rate, faster displacement of water by the extending mixing zone

and turbidity current probably caused the stronger subsequent back flow of water, which had a stronger retarding effect on the turbidity current than in deeper water.

Experimental lock-exchange liquid gravity currents controlled by buoyancy and inertial forces typically evolve through an initial phase of constant velocity, $x \propto t$, followed by a second phase of deceleration according to a $x \propto t^{2/3}$ relationship of front position, x, over time, t (Simpson 1987); such behavior has also been observed with particle-laden liquid density currents (e.g., Bonnecaze et al. 1993; McLeod et al. 1999). The log-log plot in Fig. 14b shows a turbidity current in a cool-ash run to follow a line of slope 1 ($x \propto t$) before deceleration begins and motion approaches a line of slope 2/3 more distally. The mixing zone thus is closely analogous to a reservoir of denser liquid in a lock-exchange experiment that collapses when the gate is removed (Fig. 14b); times of mixing-zone formation of around 2 s are much shorter than times of turbidity-current runout of about 20 s. Initial velocity of a turbidity current is here, however, also controlled by the inclined ramp extending through much of the length of the mixing zone (Fig. 14b). The close analogy with simple experimental gravity currents justifies the use of the velocity relation $U=(g'H)^{1/2}$ to estimate turbidity-current densities, where H is depth of the current (typically around 40% of the water depth as expected for near-inviscid currents in shallow water; Simpson 1987) and g' the reduced gravity. Turbidity-current densities thus decreased from about 1,150–1,250 kg m^{-3} proximally to <1,010 kg m^{-3} near the tank end mainly in response to sedimentation.

In hot-ash runs, where the mixing zone was made up of fountain fallout sinking through the depth of the water, a measurable turbidity-current front could only be identified over medial to distal ranges. This could be due to the front being obscured in the highly turbid proximal waters, but probably also to some time delay needed to form a proper turbidity current. Motion of its visible front was then unsteady due to frontal additions of sinking sediment plumes, giving the appearance of sudden accelerations (Fig. 14a, c). Downstream of the region of sinking sediment plumes (mainly the maximum extent of the fountain edge), which was more extensive the higher the ash temperature (Fig. 14a) or mass (Fig. 14c), the turbidity currents first strongly decelerated and then approached motion according to $x \propto t^{2/3}$ (Fig. 14a–c). The brief interval of near-stagnation (S in Fig. 14a) correlated with a major back-surge of overlying water to where water had been displaced by entry, explosions, and massive fountain fallout. Density estimates as for currents in cool-ash runs are inhibited by unsteady motion, but the higher sediment concentrations (Fig. 8) suggest higher densities of turbidity currents in hot-ash runs. At shallow water depths, propagation of a turbid front under water was completely controlled by fallout from ash fountains and the ash-cloud surge; Fig. 14d shows how closely the turbid front trailed the ACS. Turbidity currents did not develop at water depths D=4–8 cm in experiments using hot ash.

Liquid–particle gravity currents in which the liquid is less dense than the ambient water (McLeod et al. 1999) dilute by sedimentation during runout until they become positively buoyant. Turbidity currents in the experiments reported here were always warmer than the tank water, but never lifted off the floor within the length of the tank; such behavior did occur, however, in experiments using coarser material, which will be reported elsewhere.

Ash-cloud surges

Ash-cloud surges generated at the point of entry in cool-ash experiments decelerated rapidly from initial speeds of about 1 m s^{-1}. Such high initial speeds suggest some momentum was transferred from the granular flows (around 2 m s^{-1}) to the ash-cloud surges. Subsequent deceleration was more gradual (Fig. 15a) and approached a $x \propto t^{2/3}$ relationship (Fig. 15c). Using shallower water had no significant effect on ash-cloud spreading in cool-ash runs (Fig. 15a). The depth of ash-cloud surges was difficult to determine because it increased from head to tail and the surface was irregular due to turbulent billows, indicative of mixing with air. Using depth estimates taken about 20 cm behind the flow front and observed velocity values, ACS particle concentrations can be estimated from a velocity function for an intrusive gravity current (e.g., Legros and Druitt 2000, Eq. 7). Particle volume fractions in cool ash-cloud surges then appear to diminish from order 5×10^{-4} proximally to near 10^{-5} distally in the tank; the magnitude of this loss agrees with the downstream decay in ACS-sediment concentration (Fig. 10a).

Ash-cloud surges in hot-ash experiments initially spread in a similar fashion as those in cool-ash runs, but then suddenly accelerated in response to steam explosions (Fig. 15a, c). Commonly the currents decelerated from 1–1.5 m s^{-1} to about 0.5 m s^{-1} and then accelerated back to about 1 m s^{-1} while simultaneously increasing in depth. Such high velocities caused basal traction during ash deposition (Fig. 12) in contrast to "quiet" fallout from slower surges in cool-ash runs. In some experiments, video records taken from above showed how a vertically rising ash plume was suddenly sucked back down and forward; such strong downward convection was probably caused by a strong acceleration of the ash-cloud surge. The higher the ash temperature, the higher the surge velocity became and the closer to shore did the acceleration begin (Fig. 15a) since explosions started earlier, whereas variations in ash mass or mass flux did not significantly affect ACS velocities (Fig. 15b). Shallower water depths did not systematically affect ACS motion; the downstream displacement of the onset of acceleration in Fig. 15d (compared with Fig. 15a, b) may be a combined effect of a lower ash temperature and of the range of explosions being laterally more extensive in shallow water. Unsteady motion of hot ash-cloud surges inhibits estimates of particle concentrations as above for cool surges; ACS sediment concentrations (Fig. 10a) do, however, suggest up to 16 times higher surge concentra-

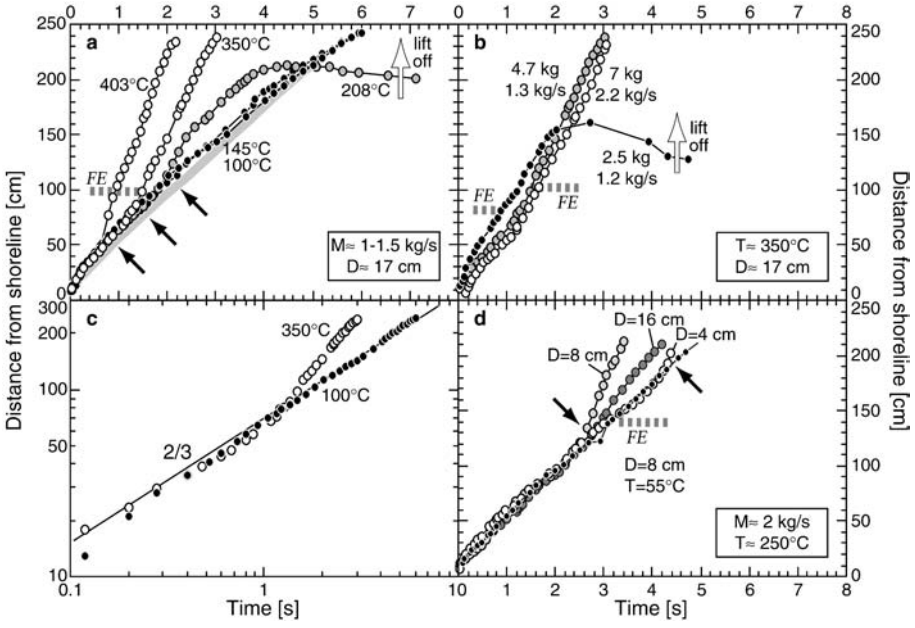

Fig. 15 Positions of ash-cloud surge fronts over time for experiments using different **a** ash temperatures, **b** ash masses, and **c** water depths. *White arrows* in **a**, **b** indicate ACS lift-off after deceleration and dilution. *Black arrows* in **a**, **d** point at onset of acceleration of hot ash-cloud surges behind fountain edges (*dashed bars*, *FE*). *Bold gray line* in **a** repeats data for D=8 cm, T=55 °C from **d** for comparison with cool-ash run data (*black dots*) at D=17 cm. **c** Log-log plot shows $x \propto t^{2/3}$ relationships analogous to Fig. 14b

tions for the hottest runs (in fact even higher since the hot ACS were faster). The surges from two experiments, one of relatively low ash temperature (208 °C, Fig. 15a) and the other of low ash mass (2.5 kg, Fig. 15b), show a spreading behavior that all hot surges would have ultimately shown had the tank been long enough. These two surges decelerated as they lost much of their load by sedimentation, finally became positively buoyant (at particle volume fractions of order $<10^{-5}$) and lifted off the water surface, the front retreating somewhat as it was sucked by the thermal draft. Such lift-off defines the runout length of hot suspension currents, which generally increases with initial mass flux (Bursik and Woods 1996; Freundt 1999).

Waves

In cool-ash runs, water was displaced near shore by the impacting granular flow of typical speed ≈200 cm s^{-1} and depth <3 cm. Legros and Druitt (2000) argued that water would be totally displaced on an inclined shore up to a distance where water depth equals flow depth (for flows denser than water), or the immersed part of flow depth (for flows lighter than water). With a loose-packed bulk density of ash of 960 kg m^{-3}, granular-flow bulk densities would be less than water density, with about 80% of their flow depth becoming immersed. Total displacement of water in our experiments would then be expected only up to about 6 cm from shore, giving a displaced water volume of 160 cm^3. The bowl-shaped depression in the water surface (Fig. 3b) typically reached <15 cm length and <3 cm negative amplitude; the resulting wave had an initial length and positive amplitude of about the same respective dimensions, corresponding to <500 cm^3 of displaced water. Legros and Druitt assumed steady-state conditions whereas here water displacement occurred impulsively, involving energetic splashing. It is interesting to note that liquid–particle gravity currents produced waves 7–10 cm high at comparable entry speeds, ramp inclination, and water depths (McLeod et al. 1999), suggesting that gas-particle flows as used here are less efficient in producing waves.

Incoming ash drastically decelerated to about 50 cm s^{-1}, judging from the initial advance rate of the mixing zone front (MZF in Fig. 4a). The wave formed by impact splashing initially moved with the mixing-zone front, but then detached and propagated faster (at about 20 cm from shore in Fig. 4a). A wave can only detach from the mixing zone where the value of the limiting rate of water displacement, $c=(gD)^{1/2}$ (which increases with water depth down the ramp up to the maximum value of <130 cm s^{-1} for water depth on the flat floor) is greater than the advance rate of the mixing zone, a condition met beyond about 5 cm from shore. In all cool-ash experiments, however, the first wave and the mixing-zone front moved together until the advance rate of the mixing zone dropped below values of 30–40 cm s^{-1} (at about 15–20 cm from shore where c=80–90 cm s^{-1}). This suggests the growing mixing zone pushed the wave until its expansion became too slow.

Subsequent waves generated at later times by arrivals of high-mass-flux pulses at shore were poorly visible in the mixing zone, but overtook its front at significantly greater speeds. Yet, even when they liberated from the mixing zone and gained speed, all waves remained slower than expected from the c-values up to the final third of the tank length, where their wavelength had increased to two to three times the initial value and trailing waves had united (Fig. 4b). Walder et al. (2001) studied wave generation by mass flows and identified an initial splashing zone (where waves are generated), a near field

(where wave motion is still affected by source dynamics), and a far field (where speed c is maintained and source dynamics are unimportant). The far field begins roughly three far-field wave lengths behind the splashing zone, i.e., at about 100 cm from shore in the present experiments, which is in good agreement with observations in Fig. 4b.

The first wave in hot-ash runs also formed by impact of the granular flow at shore and then evolved like the first wave in a cool-ash run, quickly detaching from the mixing zone. The first wave in Fig. 7a had a low amplitude of 9 mm and could not be traced far down the tank. The second wave in that experiment had an amplitude of 2 cm and appeared after a strong explosion. Several such explosion-derived waves could form in other experiments. Initially this wave had an asymmetric shape with a steep upstream flank and was immediately trailed by the tip of the sediment-plume region (SPT in Fig. 7b) that marked the extent of fallout from an ash fountain and the ash-cloud surge. The wave and the SPT both moved at a speed of 57 cm s^{-1}, much slower than expected from the value of c=128 cm s^{-1}. At about 100 cm from shore, the maximum extent of the ash-fountain edge, the wave detached from the SPT, which then trailed the ash-cloud surge (Fig. 7b). The wave accelerated to a velocity approximately equal to c and attained a symmetrical shape with about twice its initial wavelength, but with reduced amplitude. Asymmetrical shape and the pattern of motion of these explosion-derived waves suggest they were pushed up to the extent of the fountain edge before turning into liberated shallow-water waves. The ash-cloud surges with particle volume fractions probably $<5\times10^{-3}$ had an immersed depth of <1% of their total depth and transferred little momentum to the water judging from ρU^2 of order 1 Pa; they were thus unable to displace surface water to form a bow wave. Water was probably displaced by the advancing fountain edge, behind which a heavy shower of ash fell onto the water surface. These waves thus initially formed by steam expansion at a site of strong explosion and then remained driven by massive ash fallout until they outran the fountain edge.

Mixing processes

Entry, mixing, and ash-cloud formation of cool flows

The bulk density of the granular flows was slightly less than that of water, but it seems that both bulk and solids density were important during the entry process. Most of the ash initially followed a path as expected from bulk density by jetting up the upstream-facing flank of the wave of water displaced from shore. Some ash material, however, followed a path as expected from solids density by directly entering water and mixing with it (Fig. 3a, b). After this initial splashing event, the entry into water became smooth and continuous. The underwater mixing zone operated much like a hydraulic jump in that it consumed kinetic energy of the supercritical grain flows

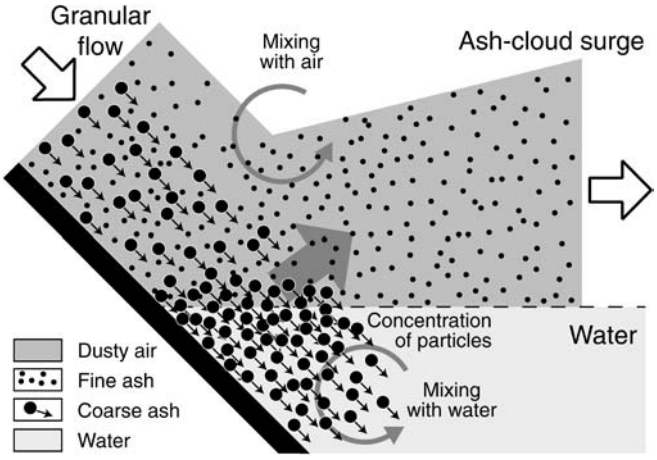

Fig. 16 Schematic illustrating the proposed unmixing of interstitial air and fine ash during mixing of mainly coarser ash with water as discussed in the text

(Froude numbers $Fr=U/(gh)^{1/2}$=2–4) by turbulent mixing. McLeod et al. (1999) observed analogous mixing zones with liquid flows of low density contrast to water, whereas denser flows continued under water more coherently.

The formation of an ash-cloud surge immediately began when a pyroclastic flow hit the water and continued until the inflow waned. The author interprets that, as the granular flows hit the water surface at an angle, the coarser particles followed a path into the water dictated by their momentum and became concentrated because their underwater velocity is much lower than that in air (Fig. 16). Low-density interstitial air of the granular flow could not enter water and escaped the only way it could go, downstream across water, taking entrained fine ash with it. The same process of ash-cloud formation was observed when granular flows hit a transverse barrier of solids on the ramp above shore, with the only difference that coarser particles stacked on the upstream side of the barrier. Noh (2000) observed experimentally that a sediment cloud of relatively coarse particles encountering a density interface sinks straight into the higher-density fluid, but a cloud of relatively fine particles spreads laterally along the interface as a density current. Experimental observations here suggest that a polydisperse sediment cloud looses its coarser load into the denser fluid while finer load and light interstitial fluid move along the density interface. The splitting of pyroclastic flows into parts moving over and under water has been commonly explained in terms of density stratification of the flows on land leading to bifurcation (e.g., Cas and Wright 1991; Carey et al. 2000), with the lower-density top part moving over water while the higher-density lower part gets submerged. The experiments here suggest an alternative explanation in that separation is controlled by properties of the phases in a two-phase flow, the density and momentum of the mixture of gas and fine ash, and of the coarser solid particles.

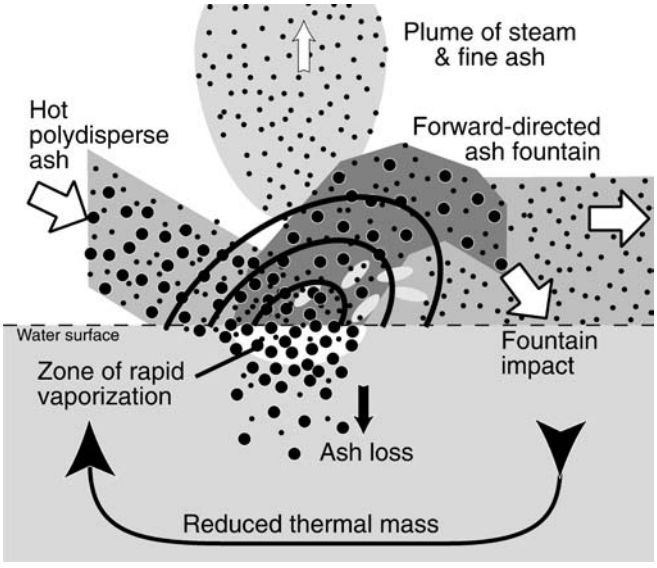

Fig. 17 Schematic illustrating the generation of steam explosions as an extension of the model in Fig. 16. Ash mass and heat are lost during repeated cycles of explosive fountaining. Pressure waves (indicated by *curved lines*) from expanding steam may be forward directed as indicated by downstream deflected fountain traces (Fig. 13) and ACS acceleration (Fig. 15). Waves not shown for clarity

Steam explosions and ACS formation of hot flows

The initial moment of entry of hot flows was very similar to that of cool flows. Steam explosions started, however, mostly within less than a second after entry and initial mixing with water. In contrast to cool-ash runs where the near-vertical front of the underwater mixing zone advanced from the shore, the tip of a densely turbid zone (SPT in Figs. 6, 7) rapidly advanced along the water surface in hot-ash runs while the mixing-zone front at the bottom (MZB) lagged dramatically behind. Little material thus moved down the ramp from shore under water, but most of the incoming ash moved along the water surface, passed through explosion fountains, and was rapidly transferred onto the water surface farther downstream. It is propose that, as with the model for ash-cloud surge formation (Fig. 16), it was mainly the coarser ash that mixed with near-surface water, in which it was concentrated due to about 60-times lower fall velocity (Fig. 17). This facilitated rapid heat transfer turning water in the mixture into steam. It is possible that the onset of explosive vaporization at one place triggered further vaporization in the mixture analogous to the transition from pre-mixture to fine-fragmentation phases during magma–water interaction (Zimanowski 1998). Explosive expansion of the steam then ejected a fountain of water, wet ash, and continuously incoming hot dry ash. Only a fraction of the ash available at a given place thus thermally reacted with the water while the remaining dry ash was passively ejected before mixing. This hot dry ash started the next explosion where it fell back from the fountain and impacted the water surface farther downstream (Fig. 17). These steps were repeated and the zone of explosive activity extended away from shore until cooling of ash and loss of ash into water inhibited further steam explosions. The extent from shore across which explosions occurred, therefore, was larger the higher the initial temperature and mass of the ash. Across this range, intensity of explosions varied probably because variable masses of ash were simultaneously involved in thermal mixing in a given area. Often later explosions farther out were more vigorous than initial explosions close to the shore. This may be related to increasing proportions of finer ash participating in thermal mixing farther downstream as suggested by the systematic decrease in grain size from shore of deposits on the tank floor. The center of a spherical particle of radius r, conductively adjusts to the temperature outside the particle in a dimensionless time $\tau=\kappa t/r^2=0.5$ (Carslaw and Jaeger 1959), where thermal diffusivity of order $\kappa=10^{-6}$ m^2 s^{-1}. Ten times larger particles thus require 100 times longer cooling. Assuming that such cooling times determine the rate of steam formation, steam would be produced much faster when the mixture contains a higher proportion of fine ash at the same mass concentration and temperature. The initial rates of steam expansion in the hottest runs must have exceeded the fall velocity of order 10 m s^{-1} of the mudballs that were thrown out ballistically. The low angle (20–30°) mudball trajectories and fountain traces on the tank panes (Figs. 11 and 13) suggest a downstream directed expansion of steam during explosions, possibly caused by the lateral influx of ash into the explosion sites. Such lateral expansion may have contributed to the acceleration of the ash-cloud surges (Fig. 15), together with their increased density.

The detailed nature of the mixing conditions generating steam explosions cannot be identified by the present data, but is the subject of ongoing investigations. Least requirements are that sufficient heat is transferred to the water and that this transfer occurs at "explosive" rates facilitated by efficient exposure of the ash-particles' surface to the water (cf. Zimanowski 1998). Thermal mass balancing, assuming perfect mixing, can be used to constrain some mixing conditions. The equation of conservation of heat

$$(1-X)\left[C_{pw}(T_b-T_w)+\alpha L_b+C_{pv}(T_m-T_b)\right] + XC_s(T_m-T)=0$$

where X mass fraction of ash in ash-water mixture, T_b boiling temperature (100 °C), T_w initial water temperature, T initial ash temperature, T_m mixing temperature, C_{pw} and C_{pv} specific heats at constant pressure of water and vapor, C_s specific heat of ash, α the mass fraction of water that vaporizes, L_b the latent heat at boiling temperature, can be solved for three cases (cf. Koyaguchi and Woods 1996): (1) all water vaporizes at large values of X, so $\alpha=1$; (2) only a fraction $0<\alpha<1$ of the water vaporizes at intermediate values of X and mixing temperature $T_m=T_b$ throughout this interval; (3) no vaporization occurs ($\alpha=0$) at low values of X and the

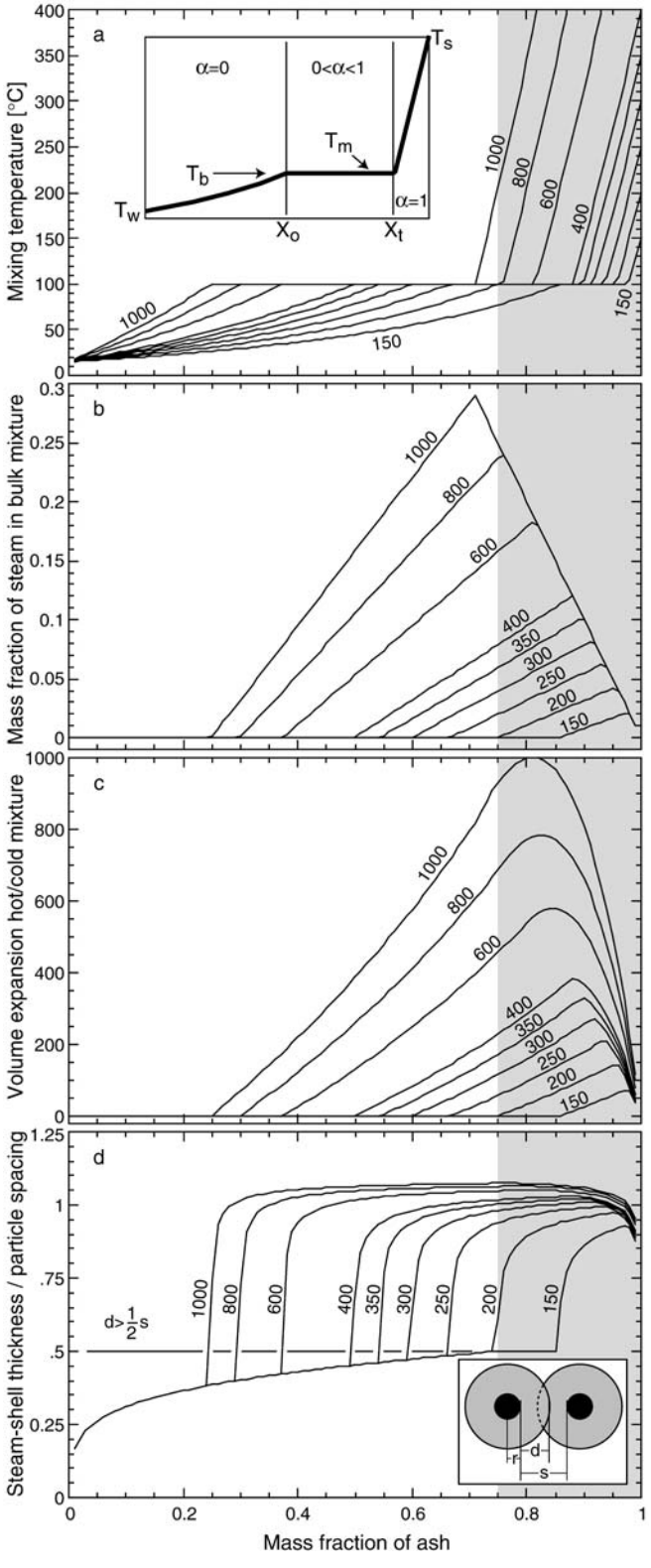

Fig. 18 Variations in **a** mixture temperature, **b** mass fraction of steam, and **c** factor of volume expansion with ash mass fraction in the mixture with water for various initial ash temperatures (°C). *Gray shading* covers mass fractions exceeding close packing that cannot be realized in particulate material but, e.g., during magma–water interaction or in hot porous rock. *Inset* in **a** illustrates three regimes of no, partial, and total vaporization. **c** Maximum volume expansion inferred for experiments (T=403 °C) is about factor 200, but almost factor 1,000 may be reached in very hot natural flows implying relatively more vigorous steam explosions. **d** Variation of the ratio of steam-shell thickness to mean particle spacing over ash mass fraction for the simple geometric assumption illustrated in the *inset* and discussed in the text. The condition $d>0.5$ s for steam coalescence is easily satisfied when vaporization occurs. The calculations used C_{pw}=4216 J/kg °C, C_{pv}=2,060 J/kg °C, C_s=1,200 J/kg °C, $L_b=2.28\times10^6$ J/kg, and gas constant R_v=500 J/kg °C; variations with temperature of C_{pw}, C_{pv}, R_v are ignored, but would not affect the results at the precision required here

second (latent heat) and third (steam heating) terms in the left bracket must be dropped. Figure 18a shows mixing temperatures as a function of ash mass fraction for various ash temperatures. As illustrated in the inset, mixing temperature increases with ash mass fraction until vaporization commences and mixing temperature remains constant at the boiling temperature because excess heat of the ash is used for the water–steam phase change. The minimum ash mass fraction for onset of steaming (X_o) decreases to higher ash temperatures. Ultimately all water vaporizes and mixing temperature rises with the ash mass fraction because excess heat is now used to heat the steam. The minimum ash mass fraction for total vaporization (X_t) also decreases with higher ash temperatures. The mass fraction of steam in the mixture at T_m increases through the range $X_o<X<X_t$ to a maximum value that increases with ash temperature (Fig. 18b), which is why explosions in the experiments were more vigorous at higher temperatures. Correspondingly, the volume of the mixture expands (assuming atmospheric pressure), reaching maximum expansion at ash fractions $X>0.8$ (Fig. 18c). However, it must be remembered that ash mass fractions cannot exceed a value of about 0.75 of closest packing; conditions at $X>0.75$ thus cannot be realized with particulate material. Therefore, steaming can only occur at ash temperatures >200 °C (Fig. 18b) and this explains why experimental steam explosions did not occur at $100<T<200$ °C. Walder (2000a, 2000b) also observed experimentally that hot sand emplaced on snow only became steam-fluidized at sand temperatures >200 °C.

Considering a simplified microscopic view in which equal-size particles are evenly spaced a distance s from each other (where s is determined by particle volume fraction relative to close packing where s=0), the vaporized mass of water may form a shell of steam of thickness d around each particle, where d can be obtained from volume expansion (Fig. 18c). When d=0.5 s, steam shells touch and the total volume of steam coalesces, facilitating immediate steam explosion of the mixture, whereas a bubbling mixture may result from $d<0.5$ s. Even for the lowest steam-forming ash temperatures, the condition for steam coalescence is realized (Fig. 18d). It should be noted that, however, nucleate boiling (small steam bubbles form at, and detach from, the particle surface) in fact occurs at relatively low temperatures (Walder 2000b) so that the simple geometry assumed here would not be valid.

Experimental limitations and applications to nature

There are some major differences between experiment and nature that need to be considered when applying the observations made. Variable coastal geometries from near-horizontal beaches to vertical sea-cliffs will modify the entry process. In the first case, pyroclastic flows will probably override or displace very shallow water and only form a mixing zone as observed here where water gets deeper. In the second case, pyroclastic flows will especially loose heavy components during their jump over the cliff, but then dive onto water and mix. Radial spreading of 3-D pyroclastic flows on land and water, in contrast to the channelized 2-D experimental conditions, mainly has the effect to reduce local flow thickness and mass flux, implying quantitative, but no qualitative differences in behavior. In terms of scaling, the experimental pyroclastic flows had somewhat lower dimensionless fluxes q^* and significantly higher values of N_P (Table 2), deficiencies that are due to lower velocity (q^*) and lower thickness (N_P, q^*) compared with natural flows. Experimental flow velocities, however, are on the right scale as shown by the Fr*-values (Table 2). It is mainly the difference in flow thickness that has some implications for the application of the experimental results.

The separation process into underwater mixing and over-water ACS was efficient in the experiments because the granular flows were thin. It is speculated that, in thick flows, especially those capable of maintaining pore pressure, i.e., having a low value of the parameter N_P (Table 2), only some topmost fraction of the thickness may be affected by such separation while lower parts of the flow may wholly submerge into water. Massive deposition on the ramp of ash containing air showed imperfect mixing with water in some high-ash-mass runs. Rapid overturn of such unstable deposits destroyed the initial massive deposit structure, but still thicker flows might have been able to emplace massive tuff below shoreline by displacing near-shore water. Models of pyroclastic-flow entry into the sea, however, assume a smooth transition of the bulk flow from land into water (e.g., Sparks et al. 1980); such wholesale intrusion did not occur in the experiments up to the maximum values of H/D=0.4 and 0.6 for cool-ash and hot-ash runs.

The thermal mixing situation as in Fig. 17 may be envisioned as a permeable package of hot ash being invaded by a planar water front. Woods and Fitzgerald (1993) analyzed the unidirectional intrusion of a planar water-front at steady rate into hot porous rock. They distinguished two cases: (1) the intrusion rate of water is low and the water fraction vaporized at the interface only depends on rock temperature, and (2) the intrusion rate is so high that steam diffuses too slowly away from the interface and accumulates, to the effect that the mass fraction of water getting vaporized decays rapidly with time. High permeability and porosity and little overburden pressure during ash intrusion into water in the experiments probably always allowed free expansion of the steam from the interface. In the case of thick, high-mass-flux, low-N_P natural pyroclastic flows, however, steam diffusion might have a limiting effect. Steam explosions then must be generated shortly after onset of thermal mixing, or will not occur at all, because the efficiency of vaporization will diminish during protracted intrusion. In any case, great flow thickness probably reduces the fraction of incoming ash that can simultaneously participate in thermal mixing at a given place. If steam explosions nevertheless occur, more hot ash will be preserved for subsequent interactions and the range of explosions would be relatively extended from shore.

One or more explosions occurred in all hot-ash runs; the fact that geologic evidence for such explosions is almost never reported may be explained by most of the erupted material passing through low ash fountains only to re-enter the sea and become mixed with the material flowing under water. Only a small mass fraction of ash is more widely distributed, possibly on land, by the convective plume, but such ash layers are difficult to identify and have a low chance of preservation. Acceleration of the ash-cloud surge to twice its velocity, but only very minor steam explosions, have been observed upon entry of pyroclastic flows into the sea at Montserrat (Cole et al. 1998), probably because the flows were not very hot (<250 °C) and slow (8–15 m s^{-1}), only reaching 200 m out to sea.

Some of the experimental observations made here differ from results obtained in experiments using analogue liquids. Whether ash transport was mainly into water or along the water surface was determined by ash temperature because there was no apparent difference in bulk density of cool and hot granular flows in the experiments, while analogue–liquid experiments identified flow density (relative to water) as the major control (Cas et al. 1998). Legros and Druitt (2000) used ground-hugging carbonate-solution density currents that chemically reacted with acid ambient water producing CO_2-bubbles as a simulation of steam generation. The hot-ash experiments showed that, however, thermal interactions occur along the water surface rather than inside the water column.

Conclusions

I have reported new experimental observations of phenomena that occur when pyroclastic flows enter the sea. By using "real" hot pyroclastic flows it was possible to identify interaction processes that could not be observed in previous experiments using analogue isothermal particle-laden liquids. Thermal effects together with the poorly size-sorted nature of the flow material, however, mainly determine the style of interaction. The three most important differences to observations made with liquid analogue currents are that (1) dominant sediment transport along the bottom or the water surface is controlled by temperature rather than density of the incoming pyroclastic flow, (2) phreatic explosions occur by thermal

mixing at ash temperatures >200 °C, and (3) major ash-cloud surges are produced near-shore by unmixing of gas and ash while a pyroclastic flow mixes with water.

Even the entry of relatively cool pyroclastic flows into the sea generates a dilute ash-cloud surge travelling over water. The vast majority of material, however, mixes with the water. Coarse and heavy material rapidly accumulates on the near-shore seafloor, generating extensive mass slumping if bottom slope is sufficiently steep. The remaining dense ash-water mixture turns into a turbidity current forming a normally-graded, exponentially thinning extensive deposit on the seafloor, which becomes covered by pumice lapilli that were initially buoyantly separated and formed floating pumice rafts before they soaked and sunk.

Most of the material carried by hot (>250 °C) pyroclastic flows entering the sea is initially transported along the water surface. Mixing with water across the surface generates steam explosions over some distance from shore, forming lower wet and higher dry ash fountains and convective ash plumes. A highly concentrated ash-cloud surge develops upon entry and by the explosions and travels out to sea at high speed, being accelerated by the steam explosions. The surge is initially wet and highly concentrated in a lower zone, which rapidly decays by sedimentation while an upper zone is dry and more dilute, looses sediment at lower rates and decelerates less rapidly. Massive sedimentation from fountain fallout and proximal ash-cloud surge forms dense sediment plumes sinking toward the seafloor, where coarser load is dropped while finer load collects in a turbidity current.

Both cool and hot pyroclastic flows entering the sea generate waves when they impact the water. Subsequent waves can form during unsteady incoming mass flux and by steam explosions. Expansion of the underwater mixing zone of cool flows, but much more efficiently the heavy fallout from explosion fountains, further displace water out to sea up to their respective extents before waves evolve according to water depth unaffected by source conditions. The experiments reported here support that there are three major risks associated with the entrance of pyroclastic flows into the sea: pyroclastic surges over water, littoral explosions, and tsunami waves.

Acknowledgements Martin Launer's assistance in constructing and performing the experiments was invaluable. Constructive reviews of an earlier version by Joe Walder and Steve Carey were very helpful in producing the present paper. This research was funded by grants Fr947/7-1 and 7-2 from the Deutsche Forschungsgemeinschaft (DFG) to A.F.

References

Bonnecaze RT, Huppert HE, Lister JR (1993) Particle-driven gravity currents. J Fluid Mech 250:339–369

Bursik MI, Woods AW (1996) The dynamics and thermodynamics of large ash flows. Bull Volcanol 58:175–193

Carey S (2000) Volcaniclastic sedimentation around island arcs. In: Sigurdsson H et al. (eds) Encyclopedia of volcanoes. Academic Press, New York, pp 627–642

Carey S, Sigurdsson H, Mandeville C, Bronto S (1996) Pyroclastic flows and surges over water: an example from the 1883 Krakatau eruption. Bull Volcanol 57:493–511

Carey S, Sigurdsson H, Mandeville C, Bronto S (2000) Volcanic hazards from pyroclastic flow discharge into the sea: examples from the 1883 eruption of Krakatau, Indonesia. Geol Soc Am Spec Pap 345:1–14

Carey S, Morelli D, Sigurdsson H, Bronto S (2001) Tsunami deposits from major explosive eruptions: an example from the 1883 eruption of Krakatau. Geology 29:347–350

Carslaw HS, Jaeger JC (1959) Conduction of heat in solids, 2nd edn 1988. Oxford University Press, Oxford

Cas RAF, Wright JV (1991) Subaqueous pyroclastic flows and ignimbrites: an assessment. Bull Volcanol 53:357–380

Cas RAF, Monaghan JJ, Kos A (1998) Simulating the entry of pyroclastic flows into the sea. Abstract, Conference on Sediment Transport and Deposition by Particulate Gravity Currents, Leeds, p 22

Cole PD, Calder ES, Druitt TH, Hoblitt R, Robertson R, Sparks RSJ, Young SR (1998) Pyroclastic flows generated by gravitational instability of the 1996–97 lava dome of Soufriere Hills volcano, Montserrat. Geophys Res Lett 25:3425–3428

Francis PW (1985) The origin of the 1883 Krakatau tsunamis. J Volcanol Geotherm Res 25:349–363

Freundt A (1999) The formation of high-grade ignimbrites, II: A pyroclastic suspension current model with implications also for low-grade ignimbrites. Bull Volcanol 60:545–567

Freundt A, Schmincke HU (1986) Emplacement of small-volume pyroclastic flows at Laacher See (East-Eifel, Germany). Bull Volcanol 48:39–59

Freundt A, Schmincke HU (1998) Emplacement of ash layers related to high-grade ignimbrite P1 in the sea around Gran Canaria. In: Weaver PPE, Schmincke H-U, Firth JV, Duffield WA (eds) Proc Ocean Drill Program Sci Res 157:201–218

Fritz WJ, Stillman CJ (1996) A subaqueous welded tuff from the Ordovician of County Waterford, Ireland. J Volcanol Geotherm Res 70:91–106

Iverson MI, Denlinger RP (2001) Flow of variably fluidized granular masses across three-dimensional terrain, 1. Coulomb mixture theory. J Geophys Res 106:537–552

Koyaguchi T, Woods AW (1996) On the formation of eruption columns following explosive mixing of magma and surface-water. J Geophys Res 101:5561–5574

Legros F, Druitt TH (2000) On the emplacement of ignimbrite in shallow-marine environments. J Volcanol Geotherm Res 95:9–22

Mandeville CW, Carey S, Sigurdsson H, King J (1994) Paleomagnetic evidence for high-temperature emplacement of the 1883 subaqueous pyroclastic flows from Krakatau Volcano, Indonesia. J Geophys Res 99:9487–9504

Mandeville CW, Carey S, Sigurdsson H (1996) Sedimentology of the Krakatau 1883 submarine pyroclastic deposits. Bull Volcanol 57:512–529

McLeod P, Carey S, Sparks RSJ (1999) Behavior of particle-laden flows into the ocean: experimental simulation and geological implications. Sedimentology 46:523–536

Noh Y (2000) Sedimentation of a particle cloud across a density interface. Fluid Dynamics Res 27:129–142

Nomanbhoy N, Satake K (1995) Generation mechanism of tsunamis from the 1883 Krakatau eruption. Geophys Res Lett 22:509–512

Reedman AJ, Howells MF, Orton G, Campbell SDG (1987) The Pitts Head Tuff Formation: a subaerial to submarine welded ash-flow tuff of Ordovician age, North Wales. Geol Mag 124:427–439

Rottman JW, Simpson JE (1989) The formation of internal bores in the atmosphere: a laboratory model. Q J Meteorol Soc 115:941–963

Schmincke H-U, Sumita M (1998) Tephra event stratigraphy and emplacement of tephra layers, Mogan and Fataga stratigraphic intervals. Part II: Origin and emplacement of volcaniclastic

layers. In: Weaver PPE, Schmincke HU, Firth JV, Duffield W (eds) Proc Ocean Drill Program Sci Res 157:267–291
Sigurdsson H, Cashdollar S, Sparks RSJ (1982) The eruption of Vesuvius in AD 79: reconstruction from historical and volcanological evidence. Am J Archaeol 86:39–51
Simpson JE (1987) Gravity currents in the environment and the laboratory. Wiley, New York, pp 1–244
Sparks RSJ, Sigurdsson H, Carey SN (1980) The entrance of pyroclastic flows into the sea. II: Theoretical considerations on subaqueous emplacement and welding. J Volcanol Geotherm Res 7:97–105
Tinti S, Bortolucci E, Chiavettieri C (2001) Tsunami excitation by submarine slides in shallow-water approximation. Pure Appl Geophys 158:759–797
Ui T, Suzuki K, Walker GPL (1983) Flow lineations of Koya low aspect-ratio ignimbrite, south Kyushu, Japan. EOS 64:876
Walder JS (2000a) Pyroclast/snow interactions and thermally driven slurry formation. Part 1: Theory for monodisperse grain beds. Bull Volcanol 62:105–118
Walder JS (2000b) Pyroclast/snow interactions and thermally driven slurry formation. Part 2: Experiments and theoretical extension to polydisperse tephra. Bull Volcanol 62:119–129
Walder JS, Sorensen OE, Watts P (2001) Water waves generated by subaerial mass flows. J Geophys Res (in press)
Walker GPL (1979) A volcanic ash generated by explosions where ignimbrite entered the sea. Nature 281:642–646
Whitham AG (1989) The behaviour of subaerially produced pyroclastic flows in a subaqueous environment: evidence from the Roseau eruption, Dominica, West Indies. Mar Geol 86:27–40
Whitham AG, Sparks RSJ (1986) Pumice. Bull Volcanol 48:209–223
Woods AW, Fitzgerald SD (1993) The vaporization of a liquid front moving through a hot porous rock. J Fluid Mech 251:563–579
Yokoyama I (1987) A scenario of the 1883 Krakatau tsunami. J Volcanol Geotherm Res 34:123–132
Zimanowski B (1998) Phreatomagmatic explosions. In: Freundt A, Rosi M (eds) From magma to tephra: modelling physical processes of explosive volcanic eruptions. Developments in volcanology, vol 4. Elsevier, Amsterdam, pp 25–53